Journal of Colloid and Interface Science 659 (2024) 833–848

Contents lists available at ScienceDirect

Journal of Colloid And Interface Science

journal homepage: www.elsevier.com/locate/jcis

A dilute nematic gel produced by intramicellar segregation of two polyoxyethylene alkyl ether carboxylic acids

Patrick Denk [a], Lauren Matthews [b], Sylvain Prévost [b,c], Thomas Zemb [d], Werner Kunz [a,*]

[a] Institute of Physical and Theoretical Chemistry, University of Regensburg, D-93053 Regensburg, Germany
[b] ESRF – The European Synchrotron, 71 avenue des Martyrs, F-38043 Grenoble, France
[c] Institut Laue-Langevin – The European Neutron Source, 71 avenue des Martyrs, F-38042 Grenoble, France
[d] Institut de Chimie Séparative de Marcoule, BP 17171, F-30207 Bagnols sur Cèze, France

GRAPHICAL ABSTRACT

Scaled sketch of a discotic lyotropic nematic phase made of bicelles, formed when mixing two synthetic alkyl ether carboxylic acid surfactants, $C_8E_8CH_2COOH$ and $C_{18:1}E_2CH_2COOH$, in adequate mole ratios.

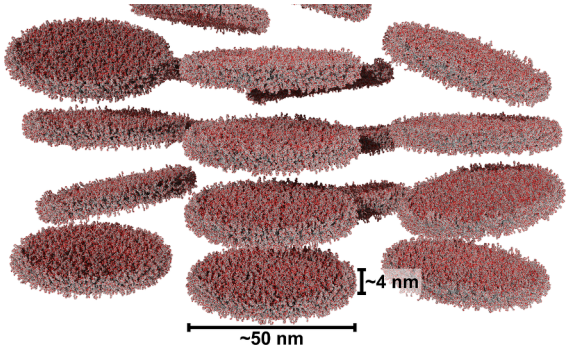

ARTICLE INFO

Keywords:
Nematic gel
Small-angle scattering
Akypo LF2
Akypo RO 20 VG
Polyoxyethylene alkyl ether carboxylic acid
Lyotropic liquid crystal
Molecular segregation
Bicelle
Discotic nematic phase

ABSTRACT

Motivation: Surfactants like $C_8E_8CH_2COOH$ have such bulky headgroups that they cannot show the common sphere-to-cylinder transition, while surfactants like $C_{18:1}E_2CH_2COOH$ are mimicking lipids and form only bilayers. Mixing these two types of surfactants allows one to investigate the competition between intramicellar segregation leading to disc-like bicelles and the temperature dependent curvature constraints imposed by the mismatch between heads and tails.
Experiments: We establish phase diagrams as a function of temperature, surfactant mole ratio, and active matter content. We locate the isotropic liquid-isotropic liquid phase separation common to all nonionic surfactant systems, as well as nematic and lamellar phases. The stability and rheology of the nematic phase is investigated. Texture determination by polarizing microscopy allows us to distinguish between the different phases. Finally, SANS and SAXS give intermicellar distances as well as micellar sizes and shapes present for different compositions in the phase diagrams.
Findings: In a defined mole ratio between the two components, intramicellar segregation wins and a viscoelastic discotic nematic phase is present at low temperature. Partial intramicellar mixing upon heating leads to disc

* Corresponding author.
E-mail address: werner.kunz@ur.de (W. Kunz).

https://doi.org/10.1016/j.jcis.2024.01.014
Received 8 December 2023; Received in revised form 28 December 2023; Accepted 3 January 2024
Available online 8 January 2024

growth and eventually to a pseudo-lamellar phase. Further heating leads to complete random mixing and an isotropic phase, showing the common liquid–liquid miscibility gap. This uncommon phase sequence, bicelles, lamellar phase, micelles, and water-poor packed micelles, is due to temperature induced mixing combined with dehydration of the headgroups. This general molecular mechanism explains also why a metastable water-poor lamellar phase quenched by cooling can be easily and reproducibly transformed into a nematic phase by gentle hand shaking at room temperature, as well as the entrapment of air bubbles of any size without encapsulation by bilayers or polymers.

1. Introduction

'Bilayer micelles', abbreviated as 'bicelles', made of bilayers of defined size limited by an outer rim, were first identified by Sanders and Schwonek in 1992 [1]. Classical bicelles are formed by mixing a long-chain lipid, such as dimyristoylphosphatidylcholine (DMPC), and a short-chain lipid, such as dihexanoylphosphatidylcholine (DHPC), in water in adequate mixing ratios. Typically, the lipid mixture forming bicelles contains around 65–85 % of the long-chain lipid [2–4]. The packing conditions can be rationalized using the geometrical chain packing model introduced by Israelachvili et al. [5]. A precise definition of the spontaneous packing parameter p_0 and a comparison with other types of packing parameters are given in **Note S1**. The long-chain lipid has a spontaneous packing parameter $p_0 \approx 1$ and favors low curvature in a bilayer packing, while the short-chain lipid has a lower p_0 and favors higher curvature. Therefore, intramicellar molecular segregation results in the formation of disc-like bicelles consisting of a bilayer disc that is limited by a half-toroidal rim. Since their discovery, bicelles have gained significant interest in biochemistry and biophysical chemistry, because they mimic biological membranes and are often orientable in magnetic fields, making them attractive vessels for NMR studies of membrane proteins [1,4,6–10]. Various different morphologies are found in systems containing disc-like bicelles, such as perforated or unperforated uni- and multilamellar vesicles, 'infinite' lamellae and perforated lamellae, branched and unbranched worm-like micelles, and ribbons [3,4,7,8,11,12]. Apart from worm-like micelles, all these structures are related as the curvature for the long-chain lipid approaches zero, the difference being the degree of intramicellar segregation of the two lipids. If the rim-forming short-chain surfactant is completely mixed into the bilayer, i.e., if there is full intramicellar random mixing, vesicles or 'infinite' lamellae are formed. Ribbons and perforated lamellae can be rationalized as intermediate states between disc-like bicelles (discs) and 'infinite' lamellae. If disc-like bicelles start to merge due to a reduction in intramicellar segregation, the remaining high curvature rims either form holes in an extended lamella or limit the bilayers into ribbons. In fact, disc-like bicelles are usually found only below the chain melting temperature of the long chain surfactant, above which other morphologies emerge [3,8]. Due to the rich phase behavior, the term 'bicelle' is often used to refer to systems made of a hydrophobic and a more hydrophilic lipid, independent of the structures' morphologies. In this work, we use the term 'bicelle' for its original disc-like morphology. Typical diameters of such disc-like bicelles are in the range of 15–50 nm, the thickness typically being around 4–6 nm [8]. Nematic or smectic phases of bicelles are often induced by bicellar orientation in strong magnetic fields [2,4,7,8,13].

Bicelles not only can be formed with lipids, but also with other synthetic surfactants, see for example ref. [14,15]. An early example of synthetic (lipid-free) bicelles with a diameter of around 50 nm made of sodium decyl sulfate, decanol, and sodium sulfate in water that can be magnetically oriented into a discotic nematic phase was given by Lawson et al. [16] and verified by others [17,18]. In fact, these synthetic bicelles, though not termed 'bicelles', were found even before the classical lipid bicelles were described. Although disc-like micelles are relatively rare, several examples are known [19–26], many of which may be considered as synthetic bicelles. Synthetic bicelles can also be formed in catanionic mixtures, for which intramicellar molecular segregation into a bilayer and a rim was shown [27–29]. If the number density of discs is sufficiently high, a discotic nematic phase is formed [20–23,25,30–32]. Usually, discotic lyotropic nematic phases are found as a transition state between an isotropic micellar phase and an 'infinite' lamellar phase, whereas calamitic lyotropic nematic phases are found between an isotropic micellar phase and a hexagonal phase made of 'infinite' rods [31,33]. The isotropic-nematic-lamaellar/hexagonal transition then involves micellar growth to increase anisotropy until the smaller micelles merge into 'infinite' lamellae or cylinders. For the system cesium pentadecafluorooctanoate/D_2O it was shown that all three phases, the isotropic phase, the discotic nematic phase, and the lamellar phase, are made of the same small (diameter $\leq$ 10 nm) disc-like micelles [34]. In this case, the isotropic-nematic-lamellar transition is rather an isotropic-nematic-smectic transition, where the lamellar phase is a smectic phase made of layered discs. Discotic lyotropic nematic phases made of discoidal micelles or bicelles are usually of low viscosity, slightly shear thinning, and only slightly viscoelastic [35–38]. Packed onion-like multilamellar vesicles (MLVs) on the other hand are known to form shear thinning viscoelastic gels that are capable of entrapping air bubbles [39–41].

Long lasting entrapment of objects between 1 μm and 1 mm in size is still a problem with classical micelles or microemulsions. Polymeric formulations have either no threshold, below which an elastic gel allows for quasi-'infinite' entrapment, or long relaxation times, making mixing difficult. In the present paper, we show that upon mixing two commercially available extended carboxylate surfactants, namely Akypo® LF2 ($C_8E_8CH_2COOH$) and Akypo® RO 20 VG ($C_{18:1}E_2CH_2COOH$), in the right concentration and temperature range, a new viscoelastic water-swollen nematic phase of synthetic bicelles is obtained. The underlying mechanism is molecular segregation inside each bicellar disc. A possible advantage of the nematic phase over packed MLVs is its continuous aqueous phase. The defects in the nematic order are spaced by at least three to five times the size of the bicelles, which are the fundamental structural units. Any object larger than the spacing between defects is efficiently entrapped, since displacement of the entrapped object requires displacement of the defects, which requires much more than 1 $k_B \cdot T$ [42]. Efficient entrapment that can be used in applications could even be experimentally proved using visible air bubbles under soft centrifugation in the presented study. A nematic phase with similar properties, obtained by mixing lauric acid, Neodol 91–8 ($C_{9\text{-}11}E_8$), and a fragrance oil, was recently reported by Tchakalova et al. [43].

In this work, we determine phase diagrams as a function of temperature, surfactant composition, and active matter concentration, covering a wide range of temperatures, the whole range of possible surfactant compositions at a fixed active matter concentration, and the whole range of active matter concentrations at a fixed surfactant composition. We identify the microstructures by means of small-angle X-ray scattering (SAXS), small-angle neutron scattering (SANS), and optical birefringence. Further, we examine the rheology of the nematic phase and the effect of NaCl and NaOH on the nematic phase formation.

2. Experimental section

2.1. Materials

The surfactants octaoxyethylene octyl ether carboxylic acid, $C_8E_8CH_2COOH$ (M = 541 g·mol^{-1}), commercialized under the name Akypo® LF2 (90.0 wt% active matter, 0.9 wt% NaCl, 9.1 wt% water), and dioxyethylene oleyl ether carboxylic acid, $C_{18:1}E_2CH_2COOH$ (M = 415 g·mol^{-1}), commercialized under the name Akypo® RO 20 VG (95.8 wt% active matter, 0.1 wt% NaCl, 4.1 wt% water), were a generous gift by Kao Chemicals GmbH (Emmerich am Rhein, Germany). The hydrophobic chain of $C_{18:1}E_2CH_2COOH$ is a mixture of various hydrocarbon chains. $C_{18:1}$ denotes an oleyl ((Z)-octadec-9-enyl) chain and is the most abundant chain with a fraction of at least 75 %. While the proportion of the (E)-isomer is unknown, the (Z)-isomer is expected to be the predominant species. Saturated myristyl, cetyl, and stearyl, as well as other unsaturated species, mainly $C_{18:x}$, make up for the other 25 % of the chains, the cetyl group being the most abundant after $C_{18:1}$ with a fraction of around 10 %. Both surfactants are technical products with a broad distribution of the degree of ethoxylation, typically containing small amounts of glycolic acid, formic acid, diglycolic acid, polyethylene glycol, carboxymethylated polyethylene glycol, nonionic polyoxyethylene alkyl ethers, and various esters of the type $C_8E_xCH_2COOE_yC_8$ or $C_{18:1}E_xCH_2COOE_yC_{18:1}$, respectively, as impurities. No differences in phase behavior were observed if using different batches of the surfactants.

Traces of remaining impurities, such as NaCl, as well as hydrophilic impurities, can be removed by cloud point extraction. For experimental details and problems arising for $C_{18:1}E_2CH_2COOH$, see **Note S2**. If not stated otherwise, to reduce the amount of hydrophilic non-surfactant impurities and NaCl, while at the same time ensuring reproducibility, $C_8E_8CH_2COOH$ was used after purification by cloud point extraction and $C_{18:1}E_2CH_2COOH$ was used as received. In the latter case, the water content was accounted for in any calculations.

A further way to purify the surfactants is to remove nonionic impurities by ion exchange. The method used and adapted in this work was described and evaluated by Cattelaens et al. [44]. Experimental details are given in **Note S2**. The process was shown to be effective for the removal of nonionic impurities from ethoxylated and non-ethoxylated carboxymethylated fatty alcohols [44]. Potentiometric pH titrations of $C_8E_8CH_2COOH$ before and after ion exchange, see **Fig. S1**, clearly indicate an increase in acid fraction. If a constant average molar mass of 541 g·mol^{-1} is assumed for $C_8E_8CH_2COOH$, an increase in acid fraction from 82 mol% to 95 mol% is obtained. Note, however, that the molar mass and its possible change during purification are not known precisely, and more analytical data would be necessary to deduce precise acid fractions. An increase of the physical density after the purification process, see section 2.5, is also in agreement with the removal of the less dense nonionic impurities.

2-propanol (p.a., ≥99.8 %) was purchased from Fisher Scientific (Pittsburgh, Pennsylvania, USA). KOH (p.a., ≥85.0 %), 1M hydrochloric acid, and squalane (for gas chromatography) were purchased from Merck (Darmstadt, Germany). 1M NaOH solution and NaCl (p.a., ≥99.5 %) were supplied by Carl Roth (Karlsruhe, Germany). D_2O (99 % D) was supplied by Eurisotop (Saint-Aubin, France). Ultrapure water from a Millipore purification system (resistivity > 18 MΩ cm) was used for all systems containing water.

2.2. Phase diagram determination

All phase diagrams were determined in a temperature range of 10 °C to 95 °C using a Julabo (Seelbach, Germany) F32-HD refrigerated and heating circulator. Occasionally, phase transitions were evaluated below 10 °C for a better determination of phase boundaries. Samples were prepared in 16x100 mm test tubes with sealed polypropylene screw caps. Prior to the recording of phase diagrams, samples were usually heated to 50 °C and mixed with a vortex mixer during re-cooling. Phase boundaries were determined by visual observation with an accuracy in temperature of ± 1 °C during heating. The temperature was adjusted in steps of 1 °C and samples were left to equilibrate for at least 10 min. An equilibration time of 10 min was found to be more than sufficient for all observed phase transitions and the same phase boundaries were found during cooling. In case of inhomogeneity, samples were agitated using a vortex mixer and left equilibrated again before evaluation of the equilibrium phase. To allow full macroscopic phase separation, some samples were left equilibrated for up to 72 h. To distinguish different liquid crystalline and isotropic phases, samples were observed between crossed polarizers. In addition, polarizing microscopy was performed using a Leitz (Wetzlar, Germany) Orthoplan polarizing microscope equipped with a JVC (Yokohama, Japan) digital camera (TK-C1380) and a Linkam (Epsom, UK) LTS350 heating/freezing stage comprising a TMS90 temperature controller (±0.5 °C) and a CS196 cooling system. To be able to investigate both phases of biphasic samples at room temperature, complete phase separation was facilitated by centrifugation with a 3-18KS centrifuge from Sigma Laborzentrifugen (Osterode am Harz, Germany).

The focus of this work is a mixture of two commercial ethoxylated alkyl ether carboxylate surfactants, namely, Akypo® LF2 ($C_8E_8CH_2$-COOH) and Akypo® RO 20 VG ($C_{18:1}E_2CH_2COOH$). In binary mixtures with water, both surfactants individually exhibit remarkably simple phase behaviors. The only feature in the phase diagram of purified $C_{18:1}E_2CH_2COOH$ in water, see Fig. 1A, is the formation of a semi-crystalline lamellar L_β phase at lower temperatures up to around 90 wt% of surfactant (2.5 water molecules per headgroup). First, increasing the water content leads to an increase of the melting temperature of the L_β phase, until a maximum of around 48 °C is reached around 80 wt% of surfactant (6 water molecules per headgroup). Further addition of water does not influence the melting temperature of the L_β phase, and a dilute aqueous phase separates from the L_β phase. This indicates that the L_β phase is most stable at a certain degree of headgroup hydration, and any excess water is expelled from the L_β phase. Depending on the hydration of the carboxylic acid group, the available number of water molecules per ethylene oxide (EO) group at 80 wt% surfactant is between 2 and 3, which is in good agreement with the most common hydration number for the inner hydration shell of EO reported in literature [45–47]. Beyond basic hydration of the headgroups, $C_{18:1}E_2CH_2COOH$ and water are not miscible. It is important to note that in most cases throughout this work, $C_{18:1}E_2CH_2COOH$ was used as received, and no L_β phase is observed without purification in the examined temperature range. The phase diagram is identical, only that the surfactant-rich phase is an isotropic liquid over the whole temperature range. Probably, the ester impurities, see section 2.1, destabilize the L_β phase.

The binary phase diagram of the more hydrophilic $C_8E_8CH_2COOH$ is shown in Fig. 1B. As discussed in detail in previous papers [48,49], $C_8E_8CH_2COOH$ does not form any liquid crystalline phases and the only observed feature is a lower critical temperature (clouding). The indicated tie lines (dotted horizontal lines) in the biphasic region were determined by measuring the water contents of the two separated phases. Note, however, that in previous papers $C_8E_8CH_2COOH$ was used as received, whereas $C_8E_8CH_2COOH$ used in this work was purified by cloud point extraction, see section 2.1. The different shape of the clouding curve is mainly caused by the removal of NaCl (initial NaCl content of 0.01 g NaCl per 1 g of surfactant) during cloud point extraction. Note that both surfactants are used in their acidic form with a pH around 2.2 at 20 wt% of surfactant. As will be elucidated in this work, the phase behavior becomes more diverse as a function of the surfactant ratio, when both surfactants are mixed. Most interestingly, a self-thickening, shear-thinning nematic gel with fast relaxation time can be obtained. In the following, the surfactant composition will be given as R($C_{18:1}E_2CH_2COOH$), where n is the amount of the respective surfactant in mol, which is calculated using the average molecular mass given in section 2.1.

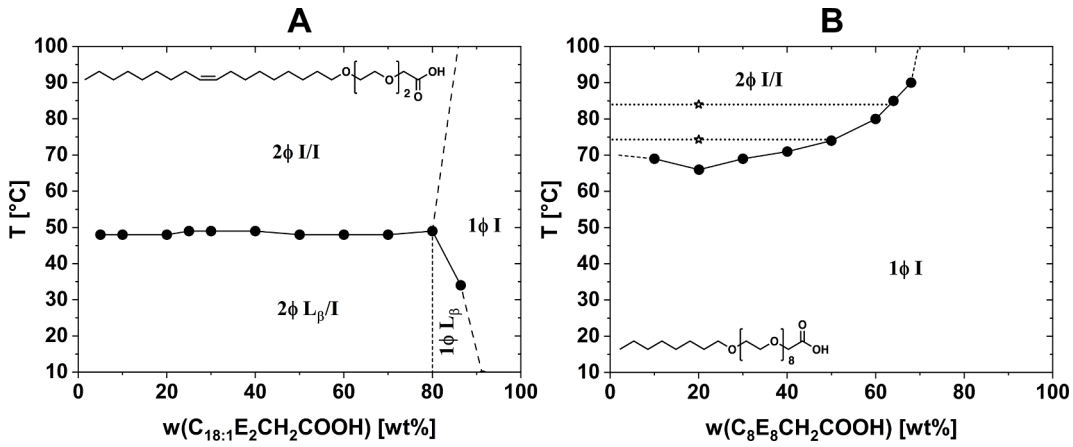

Fig. 1. (A) Binary phase diagram of Akypo® RO 20 VG ($C_{18:1}E_2CH_2COOH$) in water after purification by ion exchange and cloud point extraction. Without purification, the L_β phase is not formed within the observed temperature range, and an isotropic liquid phase is observed instead. (B) Binary phase diagram of Akypo® LF2 ($C_8E_8CH_2COOH$) in water after cloud point extraction. The two empty stars indicate points, where tie lines (horizontal dotted lines) were determined. 1ϕ I: monophasic isotropic liquid. 2ϕ I/I: two isotropic liquids in equilibrium. In the notation 2ϕ I/I, the former I regards the top phase, whereas the latter I regards the bottom phase. L_β: semi-crystalline lamellar phase. Dashed lines indicate extrapolations of the phase boundaries based on the data, but are not connecting two data points.

$$R(C_{18:1}E_2CH_2COOH) = \frac{n(C_{18:1}E_2CH_2COOH)}{n(C_{18:1}E_2CH_2COOH) + n(C_8E_8CH_2COOH)} \quad (1)$$

2.3. Small-angle X-ray scattering

Small-angle X-ray scattering (SAXS) data were performed on the ID02, TRUSAXS, beamline at the ESRF, Grenoble, France. The X-ray energy used was 12.23 keV, corresponding to a wavelength, $\lambda = 0.101$ nm. A single sample-to-detector distance of 0.8 m was used, covering a q-range of 0.072 – 7.5 nm^{-1}, where q is the magnitude of the scattering vector and is given by $q = 4\pi/\lambda \cdot \sin(\theta/2)$. All measurements were carried out in quartz capillaries of diameter $\varnothing = 1.5$ mm, with the exception of sample 20M*, for which a capillary with $\varnothing = 2$ mm was used. 2D SAXS patterns were recorded by a Dectris (Baden-Daettwil, Switzerland) Eiger2 4M pixel array detector and the sample transmission was simultaneously measured. To obtain sufficient statistics for good data quality, 12 frames of 1s exposure time were averaged, and samples underwent a radiation damage test to ensure this did not cause damage to the sample. The resulting 2D images were normalized to an absolute intensity scale and azimuthally averaged to obtain the 1D profiles. The 1D SAXS patterns were then subtracted using a capillary of water adjusted by a factor to account for the temperature. Scattering was isotropic in all cases.

2.4. Small-angle neutron scattering

Small-angle neutron scattering (SANS) data were collected on instrument D33 at the Institut Laue-Langevin – The European Neutron Source (ILL, Grenoble, France). Samples were poured in 1 mm pathway quartz cuvettes of type 120 from Hellma GmbH (Müllheim, Germany), kept on a thermalized sample-changer. A single configuration with a wavelength of 4.62 Å (relative FWHM 10 %) was used. The beam was entirely collimated, and the rear detector was placed at a distance of 13.3 m from the sample, the four front panels being at distances of 1.7 m (top and bottom) and 1.9 m (left and right). Data were processed with GRASP 10.16b [50], using the monitor as normalizer, correcting for the flat field, transmission, background noise as measured with sintered $^{10}B_4C$ at the sample position, and subtracting the contribution from a cuvette filled with D_2O. Absolute scale was obtained from the measurement of the attenuated direct beam on the detector, with a known attenuation coefficient. If not stated otherwise, given data are radially averaged. Some samples exhibit anisotropic scattering, but only the scattering intensity, not the features of the scattering curve, were found to depend on the azimuthal angle.

2.5. Density measurements

The physical densities of $C_8E_8CH_2COOH$ after cloud point extraction, vacuum dried $C_{18:1}E_2CH_2COOH$, $C_8E_8CH_2COOH$ and $C_{18:1}E_2CH_2COOH$ after purification by ion exchange and cloud point extraction, as well as various other mixtures, were measured using a density meter DMA 5000M from Anton Paar (Graz, Austria), which operates with the oscillating U-tube method. To be able to extrapolate the surfactants' densities for any temperature, the densities were measured in steps of 5 °C between 20 °C and 50 °C. A condition for each measurement was temperature stability with a maximum deviation of ± 0.002 °C. The data and their linear relations are given in **Fig. S2**.

2.6. Molecular volumes and scattering length densities

The molecular volumes and scattering length densities (SLDs) of the surfactants, also split into a hydrophobic and a hydrophilic moiety, and water (H_2O and D_2O) are given in **Note S3**, including details on their calculation.

2.7. Conductivity and potentiometric pH measurements

Potentiometric pH measurements and automated titrations were performed using a 905 Titrando high-end titrator for potentiometric titration equipped with a flat membrane pH glass electrode and an 800 Dosino dosing unit from Metrohm (Herisau, Switzerland). Conductivity measurements were performed using a conductivity measuring cell (cell constant c = 0.8 cm^{-1}) with an integrated Pt1000 temperature sensor from Metrohm. To be able to calculate the reduced molar conductivity for a titration of a sample containing 20 wt% surfactant mixture with NaCl solution, the same titration was performed with pure water as analyte. To allow for sufficient mixing during titrations involving the nematic phase, a slow titration speed, typically 0.06 mL·min^{-1}, was chosen.

2.8. Karl-Fischer titration

Volumetric or coulometric Karl-Fischer titration was used to check water contents of the surfactants and separated phases. Volumetric Karl-

Fischer titration was performed for higher water contents using a KF titrator 870 KF Titrino plus from Metrohm, while coulometric Karl-Fischer titration was performed for lower water contents using an 899 Coulometer from Metrohm, equipped with a platinum indicator and a platinum generator electrode without a diaphragm. Water contents were measured at least five times and averaged.

2.9. Threshold of bubble rising

Air bubbles of different sizes were introduced into a nematic gel containing 20 wt% surfactant mixture with R($C_{18:1}E_2CH_2COOH$) = 0.655 by simple shaking by hand. At rest, air bubbles are infinitely entrapped, i.e., they do not rise. If buoyancy is increased by centrifugation, bubbles start to rise above a certain threshold. A 3-18KS centrifuge from Sigma Laborzentrifugen, equipped with a swing-out rotor 11,180 and round buckets 13190, was used to increase the centrifugal force step by step. In total, 4 centrifuge tubes with conical bottom (15 mL) were filled with 10 mL of nematic gel each and various bubbles were monitored by taking photographs after each centrifugation step. The rotation of the rotor was increased in steps of 100 RPM at 25 °C, starting at 100 RPM. The threshold for a given bubble is then narrowed down to a range between the centrifugation step where the bubble starts to rise and the preceding step. The threshold can be used to calculate the pressure exerted by the nematic gel on the air bubble. Further details are given in **Note S4**.

2.10. Rheology

All rheological measurements were performed at 25 °C with a Kinexus lab + rotational rheometer with Peltier plate temperature control from Malvern Panalytical (Malvern, UK). Prior to sample loading, the sample was shaken by hand and air bubbles were avoided on sample loading.

A cone-plate setup consisting of an upper 40 mm stainless steel cone with an inclination angle of 4° and a stationary lower 70 mm stainless steel plate was used for recording flow curves. The gap size was set to 200 µm and shear ramps were applied with shear rates in the range of $1{\cdot}10^{-4}\ s^{-1} \leq \dot{\gamma} \leq 1000\ s^{-1}$. Typically, the shear ramp was performed within 40 min and 20 points were recorded per decade. No thixotropic or rheopectic behavior was found when first increasing the shear rate, and subsequently decreasing it.

Oscillatory rheology was performed with a parallel plate setup consisting of an upper 40 mm stainless steel plate and a stationary lower 70 mm stainless steel plate. Measurements were performed with two different gap sizes of 500 µm and 1000 µm. Strain controlled amplitude sweeps were performed to determine the linear viscoelastic region at constant angular frequencies of ω = 6.28, 10, 62.8, and 100 $rad{\cdot}s^{-1}$. Frequency sweeps were performed at constant complex strains of γ^* = 0.1, 0.2, 0.5, and 1.0 %.

3. Results and discussion

3.1. Phase diagrams

The recorded phase diagram of the $C_8E_8CH_2COOH$/$C_{18:1}E_2CH_2COOH$ surfactant mixture as a function of the surfactant composition R($C_{18:1}E_2CH_2COOH$) at a constant total surfactant content of 20 wt% is shown in Fig. 2. Both surfactants are used in their acidic form, resulting in a pH around 2.2 at 20 wt% of surfactant. The apparent pK_a of $C_8E_8CH_2COOH$ at 5 wt% of surfactant is around 3.9, the apparent pK_a of $C_{18:1}E_2CH_2COOH$ is unknown, and the apparent pK_a of the mixture with R($C_{18:1}E_2CH_2COOH$) = 0.655 at 20 wt% is around 4.6. Given the apparent pK_a of 4.6, the expected degree of acid dissociation is less than 0.5 %, rendering the surfactants with a surface charge density of less than $-1.9{\cdot}10^{-3}\ C\ m^{-2}$ pseudo-nonionic. In order to be able to assess possible influences of the nonionic impurities, especially esters, the same phase diagram was recorded using both surfactants after purification by ion exchange (see section 2.1) and is shown in **Fig. S3**. The principal phase behavior is found to be similar in both cases, the main differences being a shift of the phase boundaries to slightly higher values of R($C_{18:1}E_2CH_2COOH$) and higher temperatures after purification. As mentioned in section 2.2, $C_{18:1}E_2CH_2COOH$ purified by ion exchange can form a L_β phase in presence of water, whereas unpurified $C_{18:1}E_2CH_2COOH$ cannot.

The same is true for mixtures with R($C_{18:1}E_2CH_2COOH$) ≥ 0.9, which can form a L_β phase if the surfactants are used after purification by ion

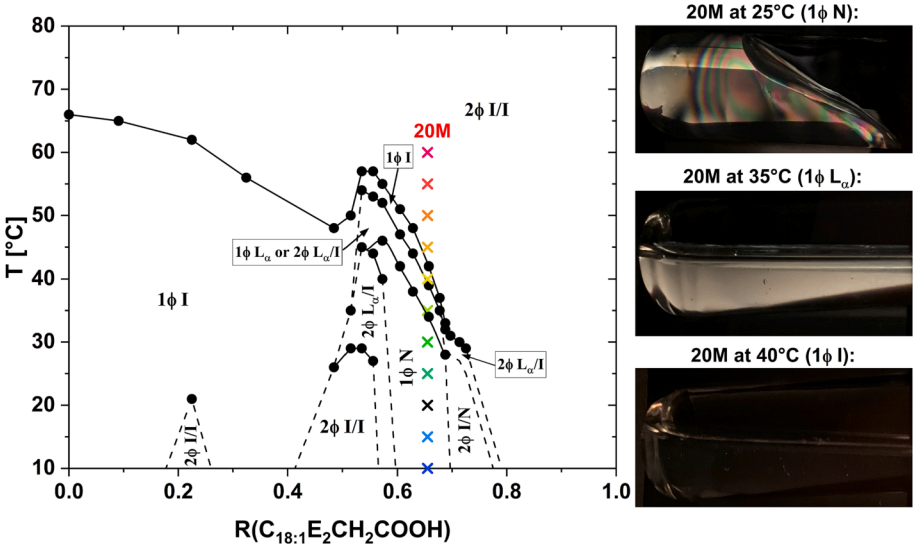

Fig. 2. Phase diagram of the $C_8E_8CH_2COOH$/$C_{18:1}E_2CH_2COOH$ surfactant mixture in water at a fixed total surfactant content of 20 wt%. The mixing ratio of the two surfactants, given as R($C_{18:1}E_2CH_2COOH$), is varied. 1ϕ I: monophasic isotropic liquid. 2ϕ I/I: two isotropic liquids in equilibrium. In the notation 2ϕ I/I, the former I regards the top phase, whereas the latter I regards the bottom phase. L_α: lyotropic lamellar phase. N: lyotropic nematic phase. The colored crosses indicate samples measured with SAXS. The three images depict sample 20M (20 wt% surfactant, R($C_{18:1}E_2CH_2COOH$) = 0.655) between crossed polarizers at 25 °C (1ϕ N), 35 °C (1ϕ L_α), and 40 °C (1ϕ I). Pictures were taken during heating of the sample from 10 °C. After 30 min of equilibration at the respective temperature, the cylindrical glass tube (diameter ≈ 1.6 cm) containing the sample was placed horizontally (perpendicular to the direction of gravity) between crossed polarizers. The same phase diagram with both surfactants purified by ion exchange is shown in **Fig. S3**.

exchange. Apart from a small biphasic isotropic domain at low temperatures around R($C_{18:1}E_2CH_2COOH$) = 0.2, which only appears in presence of the more hydrophobic ester impurities, the mixture is a single isotropic micellar phase below the critical temperature up to approximately R($C_{18:1}E_2CH_2COOH$) = 0.5. At R($C_{18:1}E_2CH_2COOH$) = 0, $C_8E_8CH_2COOH$ forms small spherical micelles (aggregation number $N_{agg} \approx 30$, radius $r \approx 2.5$ nm [48,49]) and the lower critical solution temperature (LCST) is reached at 66 °C. With increasing fraction of the hydrophobic $C_{18:1}E_2CH_2COOH$, the critical temperature decreases to 48 °C at R($C_{18:1}E_2CH_2COOH$) ≈ 0.5. It is to be expected that the two surfactants form mixed micelles, progressively deviating from the initially spherical shape. Applying the geometrical chain packing model introduced by Israelachvili et al. [5], $C_8E_8CH_2COOH$ with its short C_8 chain and large headgroup has a spontaneous packing parameter $p_0 \leq 1/3$, thus packing into spherical shape, and $C_{18:1}E_2CH_2COOH$ with its long $C_{18:1}$ chain and relatively small headgroup has a p_0 close to 1, thus favoring lamellar packing. Therefore, a progression towards an (oblate) ellipsoidal shape can be expected.

Following the transition 1ϕ I → 2ϕ I/I around R($C_{18:1}E_2CH_2COOH$) ≈ 0.5, the complete phase sequence at room temperature is 2ϕ I/I → 2ϕ L_α/I → 1ϕ N → 2ϕ I/N → 2ϕ L_α/I → 2ϕ I/I, where I denotes an isotropic, L_α a lamellar, and N a nematic phase. In the used notation, the first letter refers to the top phase, while the second letter refers to the denser bottom phase. In absence of ester impurities, see **Fig. S3**, the 2ϕ I/N domain does not appear, suggesting that the small isotropic phase contains hydrophobic ester impurities that are not solubilized in the nematic phase. Further, the nematic phase usually transitions into two isotropic phases via 1ϕ N → 1ϕ L_α → 1ϕ I → 2ϕ I/I, where 2ϕ L_α/I may appear as a coexistence domain in a narrow concentration or temperature range during the transition 1ϕ L_α → 1ϕ I. The appearance of an excess phase containing hydrophobic ester impurities in the 2ϕ I/N domain slightly alters the phase sequence. A surfactant partitioning seems to occur in the 2ϕ I/I domain above R($C_{18:1}E_2CH_2COOH$) = 0.5, where a smaller, turbid, less dense upper phase separates from a larger (≥80 vol%) bottom phase. The bottom phase at R($C_{18:1}E_2CH_2COOH$) = 0.524 contains 17 wt% of surfactant, while the top phase is richer in surfactant, suggesting that micelles in the bottom phase contain a larger fraction of the hydrophilic $C_8E_8CH_2COOH$, while the top phase is a dispersion of hydrated insoluble $C_{18:1}E_2CH_2COOH$. On heating, the mixing of the two surfactants is expected to be facilitated, explaining the transition to the 2ϕ L_α/I domain by incorporation of enough $C_8E_8CH_2COOH$ into the $C_{18:1}E_2CH_2COOH$-rich upper phase to achieve a water-soluble lamellar phase. The subsequent transition to a nematic phase can also be explained by further mixing of the two surfactants until the two separate phases, i.e., the $C_{18:1}E_2CH_2COOH$-rich lamellar top phase and the $C_8E_8CH_2COOH$-rich isotropic micellar bottom phase, merge into a single phase of mixed aggregates. At sufficient R($C_{18:1}E_2CH_2COOH$), an increase in temperature and an increase in R($C_{18:1}E_2CH_2COOH$) have similar effects.

This complex phase sequence can be rationalized by considering partial molecular segregation of the two surfactant species. Whereas there is no segregation in the isotropic mixed micellar phase for R($C_{18:1}E_2CH_2COOH$) < 0.5, on increasing R($C_{18:1}E_2CH_2COOH$) there is first intermicellar segregation into two different phases, i.e., two different microstructures, because intramicellar segregation is impossible for small spheroidal aggregates due to the cost in entropy being too high, and eventually, around R($C_{18:1}E_2CH_2COOH$) = 0.6, the two different microstructures mix to form a single species of larger aggregates, where intramicellar segregation occurs. $C_{18:1}E_2CH_2COOH$, favoring lamellar packing, is preferably populating regions of low curvature, while $C_8E_8CH_2COOH$, favoring spherical packing, preferably populates regions of high curvature. Thus, packing considerations suggest disc-like structures, also referred to as bicelles in literature. Molecular segregation was shown for catanionics [27–29], and is also the reason for the formation of bicelles when mixing a lipid with another (lipid) surfactant, which favor different curvatures [4,7–10,15]. When starting in the nematic phase, e.g., at R($C_{18:1}E_2CH_2COOH$) = 0.66 (sample 20M indicated in the phase diagram), the observed phase sequence with increasing temperature is similar to the sequence observed at constant temperature with increasing R($C_{18:1}E_2CH_2COOH$): 1ϕ N → 1ϕ L_α → 1ϕ I → 2ϕ I/I with a narrow transition zone during the transition 1ϕ L_α → 1ϕ I, where both phases are in equilibrium. This sequence can also be explained by an increase in intramicellar surfactant mixing, i.e., a decrease in intramicellar segregation, on increasing temperature or R($C_{18:1}E_2CH_2COOH$). A sufficient degree of mixing leads to merging of the bicelles into soft, highly undulating pseudo-lamellar structures, which then finally transform into mixed micelles in the isotropic phase. The eventual phase separation into two isotropic phases at a critical temperature is in most cases a classical cloud point. However, at high values of R($C_{18:1}E_2CH_2COOH$) and lower temperatures, the two surfactants possibly partition between the two phases, with an aqueous phase containing $C_8E_8CH_2COOH$-rich aggregates on the one hand and a hydrated $C_{18:1}E_2CH_2COOH$ phase on the other hand. A separation into a dilute aqueous phase and a surfactant-rich phase containing both surfactants fully mixed would then be expected at higher temperatures.

Interestingly, the clouding temperature shows re-entrant behavior: it increases from 48 °C around R($C_{18:1}E_2CH_2COOH$) = 0.5 to 57 °C at R($C_{18:1}E_2CH_2COOH$) = 0.56, before decreasing again with increasing R($C_{18:1}E_2CH_2COOH$). In absence of ester impurities, this local maximum of the critical temperature is shifted to 67 °C at R($C_{18:1}E_2CH_2COOH$) = 0.62 and almost matches the critical temperature at R($C_{18:1}E_2CH_2COOH$) = 0. The increase of the critical temperature coincides with the appearance of lyotropic liquid crystalline (LC) phases and the position of the local maximum in R($C_{18:1}E_2CH_2COOH$) matches the first appearance of the nematic phase. Critical temperatures are related to dehydration of headgroups and significantly differ for the two surfactants. In absence of intramicellar segregation, the critical temperature shows a sigmoidal shape, decreasing with increasing fraction of the hydrophobic surfactant. The intramicellar segregation present in the bicellar nematic domain is the origin of the re-entrant behavior that is clearly shown in Fig. 2.

The nematic phase is viscoelastic, capable of entrapping air bubbles, and strongly shear thinning, see rheology data in **Figs. S4 and S5**. As can be seen in **Fig. S4** and **Table S1**, the obtained flow curves of a nematic gel containing 20 wt% of surfactant mixture with R($C_{18:1}E_2CH_2COOH$) = 0.655 show two shear thinning domains that can both be fitted with the Herschel-Bulkley model [51], giving two different yield stresses, one being slightly above 1 Pa and the other one being around 10 Pa. A possible explanation for this behavior is that first larger nematic domains start to move above the first yield stress, before microscopic domains or individual discs start to move relative to each other above the second yield stress. Macroscopic viscoelasticity and air bubble entrapment can be seen in **Video S1**. Due to the shear thinning character, the gel-like mixture can be easily pipetted or mixed. After shaking of a nematic gel, bubbles are fixated instantaneously, suggesting that the viscoelastic structure is restored in less than 1s. The macroscopic appearance of a nematic gel with R($C_{18:1}E_2CH_2COOH$) = 0.655 between crossed polarizers at 25 °C can be seen in the first image in Fig. 2. When going to the pseudo-lamellar phase above 34 °C, the viscosity decreases, gel-like viscoelastic behavior is lost, and the optical appearance changes (see second image in Fig. 2). In the isotropic phase above 39 °C (see third image in Fig. 2), a low viscosity is maintained. A full sequence of images taken between crossed polarizers between 10 °C and 40 °C is shown in **Fig. S6**. Within the nematic domain, both birefringence and viscosity increase with increasing temperature.

A nematic phase is found in a range of 0.55 ≤ R($C_{18:1}E_2CH_2COOH$) ≤ 0.73, where for R($C_{18:1}E_2CH_2COOH$) ≥ 0.688 a small isotropic excess phase coexists with the nematic phase due to the presence of ester impurities, see Fig. 2. A reference mixing ratio of R($C_{18:1}E_2CH_2COOH$) = 0.655, well inside the nematic domain, was chosen so that the mixture is monophasic and nematic already at low temperatures (≥5°C). In

absence of impurities, a monophasic nematic region is observed for 0.60 ≤ R($C_{18:1}E_2CH_2COOH$) ≤ 0.90 and the reference mixing ratio was increased to R($C_{18:1}E_2CH_2COOH$) = 0.706, due to the shift of the phase boundaries to higher values of R($C_{18:1}E_2CH_2COOH$), see **Fig. S3**. Pseudo-binary phase diagrams of the surfactant mixtures in water at a constant R ($C_{18:1}E_2CH_2COOH$) = 0.655 with impurities and at a constant R ($C_{18:1}E_2CH_2COOH$) = 0.706 without impurities are given in Figs. 3 **and S7**, respectively. The principal phase behavior is the same in both cases. The nematic phase is stable in an exceptionally large concentration and temperature range, extending from 8 wt% surfactant up to around 55 wt % surfactant. Below 8 wt% (and above the critical micelle concentration), permanent birefringence and viscoelasticity are lost and the mixture is of low viscosity and flow birefringent. In presence of the hydrophobic ester impurities (Fig. 3), the flow birefringent phase is in equilibrium with a small volume of an isotropic phase, whereas in absence of the impurities (**Fig. S7**), only the flow birefringent phase is observed. Thus, the small isotropic phase found in presence of impurities is probably an excess phase, containing mainly hydrophobic ester impurities. Over the whole nematic domain, the same phase sequence as described above is found on increasing temperature: 1ϕ N → 1ϕ L_α → 1ϕ I → 2ϕ I/I with a small 2ϕ L_α/I domain during the transition between the lamellar to the isotropic phase. The lamellar phase is confirmed by polarizing microscopy, see first image in Fig. 3, where typical Maltese crosses are observed.

The phase sequence is modified above 30 wt% of surfactant, where the additional formation of a different lamellar phase prior to reaching the isotropic phase is observed at higher temperatures. The same lamellar L_α phase in equilibrium with a smaller isotropic phase is formed at room temperature on increasing the surfactant concentration beyond 55 wt%. The lamellar (smectic) nature of this phase is confirmed by polarizing microscopy, see second and third image in Fig. 3, where typical Maltese crosses can be seen before its complete melting into an isotropic phase at higher temperatures. In contrast to the lamellar phase found at lower surfactant mixing ratios, see Figs. 2 **and S3**, which is less dense than the coexisting isotropic micellar phase, the lamellar phase following the nematic phase at high weight fractions is denser than the coexisting isotropic phase. Since the surfactant mixture is only slightly denser than water if most of the $C_8E_8CH_2COOH$ is mixed with $C_{18:1}E_2CH_2COOH$, this observation suggests that the lamellar phase contains a large fraction of both surfactants. Even further increasing the surfactant concentration, a single isotropic, hydrated surfactant phase is obtained above 85 wt% of surfactant. The eventual phase separation into two isotropic phases at higher temperatures, observed up to 85 wt% of surfactant, corresponds to the classical clouding phenomenon found for nonionic ethoxylated surfactants [52], where a surfactant-rich phase separates from a dilute aqueous phase. This is confirmed by the determination of a tie-line at 20 wt% of surfactant and 60 °C, see dotted horizontal line in Fig. 3.

3.2. Dilution of bicelles to an isotropic fluid

On dilution of the nematic phase to below 8 wt% of surfactant, the nematic phase transitions into an optically isotropic fluid that is easily identified between crossed polarizers to be a flow birefringent phase. The nematic order is lost upon dilution as soon as rotational freedom is gained by an increase of the average spacing between the bicelles beyond the average diameter of the bicelles present. At rest, the mixture appears isotropic because the bicelles can freely rotate, but when applying shear, the bicelles can be momentarily oriented in the direction of the applied shear, resulting in flow birefringence. The dilute flow birefringent state can be used to analyze the form factor of the microstructures by small-angle scattering. Since the flow birefringent state is only monophasic in absence of ester impurities, samples containing 5 wt % of surfactant purified by ion exchange are used. Since the physical density of the surfactant mixture is close to 1 g·cm^{-3}, the volume fraction equals the weight fraction in H_2O.

For investigation by SAXS versus temperature, sample 5M_a_0.706 was used, where '5M' stands for 5 vol% surfactant mixture in H_2O, 'a' indicates that only the carboxylic acid surfactants after purification by ion exchange were used, and R($C_{18:1}E_2CH_2COOH$) = 0.706. Scattering was recorded at various temperatures between 5 °C and 60 °C. The

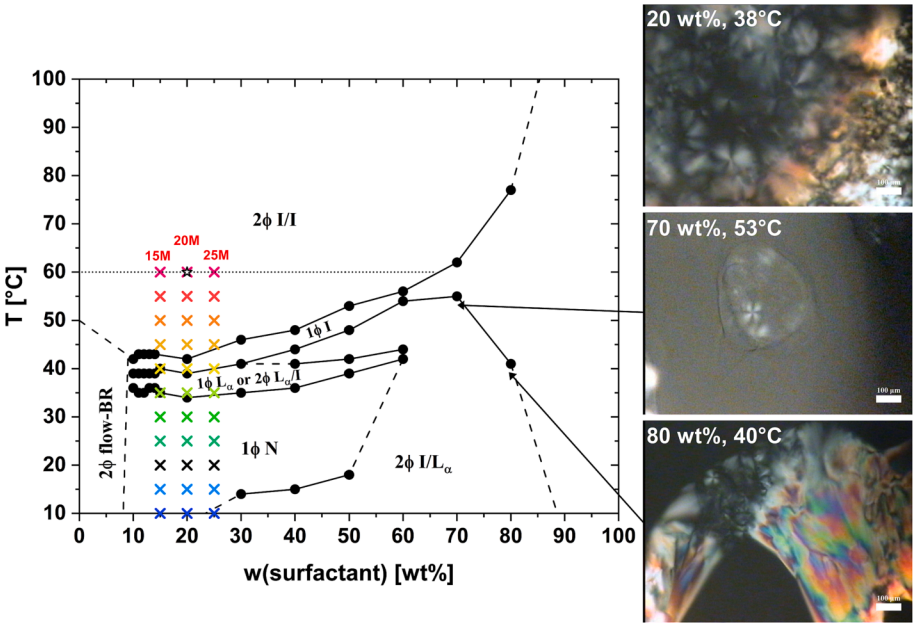

Fig. 3. Pseudo-binary phase diagram of a $C_8E_8CH_2COOH$/$C_{18:1}E_2CH_2COOH$ surfactant mixture with a fixed surfactant composition R($C_{18:1}E_2CH_2COOH$) = 0.655 in water as a function of the surfactant concentration. 1ϕ I: monophasic isotropic liquid. 2ϕ I/I: two isotropic liquids in equilibrium. In the notation 2ϕ I/I, the former I regards the top phase, whereas the latter I regards the bottom phase. L_α: lyotropic lamellar phase. N: lyotropic nematic phase. Flow-BR denotes flow birefringence. The colored crosses indicate samples measured with SAXS using a color code related to temperature increase. The empty star indicates a point, where a tie line (horizontal dotted line) was determined. The shown polarizing microscope images were taken between crossed polarizers at a 100x magnification and sample thicknesses of 0.48 mm (70 wt%) and 0.96 mm (20 wt% and 80 wt%). The scale bars indicate a length of 100 µm. A similar phase diagram with both surfactants purified by ion exchange is shown in **Fig. S7**.

resulting scattering curves are shown in Fig. 4**A**. The respective points in the phase diagram are indicated in **Fig. S7**. As can be seen in the phase diagram, the critical clouding temperature is reached at 62 °C and sample 5M_a_0.706 is monophasic and flow birefringent over the whole temperature range covered by SAXS.

The scattering curves represent a form factor oscillation with a constant position of the maximum around q = 1.1 nm^{-1} over the whole temperature range. At 5 °C, there is a sharp local minimum around q = 0.30 nm^{-1}, and probably a sharp second local minimum around q = 4 nm^{-1} that is not resolved. Up to 20 °C, the minima stay sharp, while the first one slightly shifts to approximately q = 0.23 nm^{-1}. Further increasing the temperature leads to an increasingly less pronounced form factor oscillation with increasingly flat minima. At 40 °C, only a weak first local minimum is observed at q = 0.20 nm^{-1} and a still sharp second local minimum is resolved for the first time around q = 4 nm^{-1}. For the highest measured temperature 60 °C, which is close to the critical solution temperature, the minima are still at a similar position but are much weaker compared to lower temperatures. The flattening of the minima suggests an increasing variation in aggregate thickness with increasing temperature. The oscillation in the form factor and the exact positions of the minima originate from the core–shell structure of the aggregates [53]. Changes of the structure factor can be excluded as the reason for the flattening of the minima, since the region sensitive to the structure factor is at lower q (<0.1 nm^{-1}). This can be seen in Fig. 4**B**, where deviations from the form factor fits occur only at low q. The increasing variation in apparent aggregate thickness is a result of a decreasing intramicellar molecular segregation of the two surfactant species $C_8E_8CH_2COOH$ and $C_{18:1}E_2CH_2COOH$ with increasing temperature. In the case of bicelles, i.e., discs with a $C_{18:1}E_2CH_2COOH$-rich flat bilayer part and a $C_8E_8CH_2COOH$-rich curved rim, decreasing segregation leads to an increasing bicelle radius because less relative volume of rims results in larger discs. However, despite being partially mixed into the flat bilayer part, $C_8E_8CH_2COOH$ with its much larger headgroup still is the main component of the rims. Thus, mixing of the two surfactants with big and small headgroups may be the origin of strong fluctuations, i.e., undulations, in the bilayer part.

The overall scattering contrast is quite low for X-rays, but several orders of magnitude higher for neutrons. Additionally, SAXS is highly sensitive to the internal core–shell structure, whereas SANS better probes the overall structure. Therefore, SANS of sample d-5M_a_0.706, a sample in D_2O equivalent to sample 5M_a_0.706 in H_2O, was recorded at 20 °C. 'd-5M' denotes that 5 vol% of surfactant mixture are dissolved in D_2O. The phase behavior in D_2O was found to be identical with a significant general decrease of the critical temperature and all other phase transition temperatures. In **Fig. S8**, a partial phase diagram covering different mixing ratios of the surfactants at a constant surfactant content of 20 vol% (≈18.4 wt%) in D_2O, using surfactants purified by ion exchange, is compared to the same phase diagram at 20 vol% (≈20 wt%) of surfactant in H_2O. It is important to note that the difference is caused by a solvent effect and not by a pH effect, as the equivalent pH in D_2O is only slightly increased from around 2.2 to around 2.4. The reading of the electrode calibrated in H_2O, pH*, was converted to the equivalent pH using ref. [54]. For sample d–5M_a_0.706, the critical temperature is only 50 °C, compared to 62 °C for 5M_a_0.706. The neutron scattering is shown in a Kratky-plot in Fig. 4**B** and is directly compared in log-scale to the X-ray scattering of the equivalent sample in H_2O in Fig. 4**C**. The SANS curve follows a q^{-2} slope in the mid-q range (0.06–1.5 nm^{-1}). In the absence of long-range interference effects, such as Ornstein-Zernike [55], this demonstrates the presence of large two-dimensional aggregates: finite discs, large sheets, or ribbons. With the background knowledge of the phase diagrams of the two surfactants and their mixture in water, this is only compatible with the presence of disc-like bicelles. The Kratky-representation allows for a more detailed look and is used to compare the SANS data of d–5M_a_0.706 at 20 °C to the data obtained for two additional samples with different surfactant mixing ratios, see Fig. 4**B**. The samples d–5M_a_0.677 and d–5M_a_0.750 contain 5 vol% of surfactant mixture in D_2O, where $R(C_{18:1}E_2CH_2COOH)$ = 0.677 and 0.750, respectively. Solid lines represent best fits to an oblate core–shell ellipsoid form factor using the SasView package (version 5.0.4) [56]. Details about fitting and obtained parameters are given in **Fig. S9** and **Table S2**. To avoid producing excellent fits with unphysical packings by freely varying too many parameters [57], a constrained fitting approach, as initiated by Hayter [58], is adopted. Constraints are imposed by SLDs and micellar radii that must be self-consistent with known molecular volumes and electronic densities, see **Note S3**. In all three cases, the best fit suggests a polar hydrophobic core radius close to 2 nm, corresponding to the length of an oleyl $C_{18:1}$ chain [59,60]. It is worth noting that the fit is sensitive to the polar core radius, which is visualized by the simulation (dashed line) in Fig. S9A. The hydrophilic shell thickness is similar in all cases and varies from 2.3 nm along the equatorial half-axis to 0.9 nm along the polar half-axis, in good agreement with, respectively, the lengths of the $–E_8CH_2COOH$ and $–E_2CH_2COOH$ headgroups. The length of the EO-chain in the liquid state is intermediate between the fully extended length (zigzag conformation), which is about 3.3 nm for $–E_8CH_2COOH$ and 1.1 nm for $–E_2CH_2COOH$, and the meander conformation, which is about 1.9 nm for $–E_8CH_2COOH$ and 0.6 nm for $–E_2CH_2COOH$ [61]. The only parameter that changes between the three surfactant mixing ratios is the equatorial core radius. For $R(C_{18:1}E_2CH_2COOH)$ = 0.677, an equatorial core radius of 23.8 nm is found, which increases to 24.6 nm at $R(C_{18:1}E_2CH_2COOH)$ = 0.706, and to 27.1 nm at $R(C_{18:1}E_2CH_2COOH)$ = 0.750. Since the obtained micellar dimensions reflect the molecular dimensions of the two surfactants, these results are fully consistent with intramicellar segregation of $C_8E_8CH_2COOH$ and $C_{18:1}E_2CH_2COOH$,

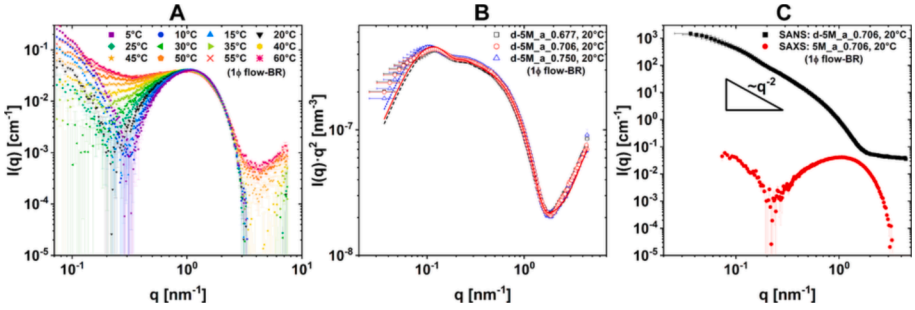

Fig. 4. (A) SAXS data of sample 5M_a_0.706, containing 5 vol% surfactant mixture purified by ion exchange with $R(C_{18:1}E_2CH_2COOH)$ = 0.706 in H_2O, at different temperatures between 5 °C and 60 °C. (B) SANS data of samples d–5M_a_0.677 (black), d–5M_a_0.706 (red), and d–5M_a_0.750 (blue) at 20 °C represented in a Kratky plot. All three samples contain 5 vol% of surfactant mixture purified by ion exchange in D_2O. The composition of the surfactant mixture is varied so that $R(C_{18:1}E_2CH_2COOH)$ equals 0.677, 0.706, and 0.750, respectively. The lines represent best fits to an oblate core–shell ellipsoid form factor for d–5M_a_0.677 (dashed line), d–5M_a_0.706 (solid line), and d–5M_a_0.750 (dotted line). For details, see **Fig. S9 and Table S2**. (C) Comparison of SANS of sample d–5M_a_0.706 (black) and SAXS of sample 5M_a_0.706 (red).

where $C_{18:1}E_2CH_2COOH$ favors the polar positions of low curvature and $C_8E_8CH_2COOH$ favors the equatorial positions of high curvature. The increase of the equatorial radius with increasing fraction of $C_{18:1}E_2CH_2COOH$ can also be explained by molecular segregation, because additional $C_{18:1}E_2CH_2COOH$ favors the flat inner part of the oblate ellipsoid, consequently increasing its size. Due to the large aspect ratio (≥12), these oblate ellipsoids resemble discs. However, the actual structure of the discs may also differ from an oblate ellipsoid. Instead of an oblate ellipsoid, where the hydrophobic core thickness, i.e., the polar radius, gradually decreases towards the equatorial half-axis, a flat cylindrical disc of constant thickness with an elliptical rim, i.e., a bicelle, would also be feasible. Both geometries are ideal cases and, in reality, the structure might be intermediate between the two ideal geometries. Further deviations from a perfectly uniform structure can be expected due to local variations in thickness of the flat disc part as a result of local molecular segregation. Local molecular segregation leads to the formation of regions of higher curvature, which can either be bumps protruding from the discs, or small holes perforating the disc. The latter can be rationalized as a rim of higher curvature, forming not only on the edge of the disc but also inside the disc.

Perforated lamellar (also named “mesh” phases) and disc-like structures have been reported in literature as intermediate states in phase sequences involving discs [62–66]. As suggested by SAXS, see above, these variations increase with increasing temperature, leading to variations in the layer thickness, i.e., undulations. It remains unknown, whether the formation of possible perforations is favored or disfavored with increasing temperature, though a decrease in segregation with increasing temperature should destabilize the internal rims and therefore the perforations. Despite the possible deviations from a perfect bicellar structure, the discs are formed due to the two opposing curvature contributions of the two surfactants, fully justifying the use of the term ‘bicelle’ in this work.

As can be seen in Fig. S9B, the basic shape of the SANS form factor can also be described with an inhomogeneous lamella form factor, which, however, fails to fit all the features of the data, including the minimum in the Kratky-plot. The best fit, reproducing at least the correct position of the kink in scattering around $q = 1.8\ nm^{-1}$, i.e., the minimum in the Kratky-plot, gives a bilayer half-thickness of 1.2 nm. Such a small half-thickness compared to the usual length of 2 nm for a $C_{18:1}$ chain is only possible if the alkyl chains are interdigitated. Interestingly, 1.2 nm is almost precisely the length of a C_8 chain [67], reducing chain packing constraints for mixing the two surfactants in a microstructure. A non-interdigitated half-thickness of 2 nm would shift the position of the minimum to lower q, as visualized by the simulation given as a dashed line in Fig. S9B. In fact, alkyl chain interdigitation is also required in the proposed oblate ellipsoid, because only the polar half-axis matches the $C_{18:1}$ chain length of 2 nm, but the thickness of the core decreases towards the equator of the ellipsoid. Thus, the $C_{18:1}$ chains can be safely considered to be nearly fully interdigitated. A tendency towards interdigitation of the oleyl chain can also be inferred from the polymorphism of oleic acid crystallization close to the melting point. The crystalline α and γ phases comprise stacks of oleic acid bilayers with separated carboxylic acid and methyl group planes, whereas the β phase comprises a layered structure of fully interdigitated oleic acid molecules. In the latter, carboxylic acid groups and methyl groups are alternating in the same plane instead of forming two separate planes [68,69].

3.3. Effect of temperature on the nematic gel

After the identification of the form factor in the previous section, in this section the effect of temperature on the nematic gel is elucidated. A viscoelastic, gel-like nematic phase with permanent birefringence is formed above 8 wt% and up to about 55 wt% of surfactant, see Fig. 3. SAXS data of sample 20M, recorded during a temperature scan from 5 °C to 60 °C, are shown in Fig. 5. Sample 20M contains 20 vol% (=20 wt%) of surfactant mixture with the ‘reference’ surfactant composition R ($C_{18:1}E_2CH_2COOH$) = 0.655 in H_2O and has a pH of 2.24. The measured points are indicated as colored crosses in the phase diagrams in Figs. 2 and 3. From 5 °C to 30 °C, the mixture is a nematic phase, and a structure factor peak is seen in SAXS. The structure factor peak is barely visible at 5 °C and becomes more pronounced with increasing temperature, suggesting that the ordering of the bicelles increases with increasing temperature. This finding is in agreement with the macroscopic observation of increasing birefringence and increasing viscoelasticity with increasing temperature and corresponds to an increase of the average bicelle diameter with temperature. When the disc diameter increases, the rotation of the bicelles is progressively more hindered as the diameter grows in relation to the average spacing of the bicelles. The increase in size on the other hand can be explained by a decrease in molecular segregation of the two surfactants. With increasing temperature, more $C_8E_8CH_2COOH$ molecules are incorporated into the flat part of the bicelle, which decreases the volume fraction of the rim and leads to a growth of the bicellar diameter. Up to 25 °C, the peak position is rather constant at $q = 0.280\ nm^{-1}$, corresponding to a repeat distance of $D^* = 22.4$ nm, which is smaller than the outer radius of around 26 nm obtained from the form factor in SANS at 20 °C. Therefore, bicelles with an equatorial radius of 26 nm seem to be a reasonable assumption even at higher concentrations and in H_2O. However, it should be noted that the total surfactant concentration and the change of solvent from H_2O to D_2O can influence the size of the bicelles. In surfactant systems, the average size of aggregates tends to increase with increasing surfactant concentration [34]. On the other hand, a decrease in diameter of classical lipid bicelles with increasing lipid concentration was reported. The influence of concentration on bicellar size is, however, small compared to the effect of the lipid composition [8,12]. An increase of the average diameter beyond 26 nm with increasing surfactant concentration is to be expected in the presented system, as the nematic phase exhibits significant viscoelastic gel-like behavior (**Fig. S5**), suggesting that the disc radius is considerably larger than the repeat distance of 22.4 nm. A

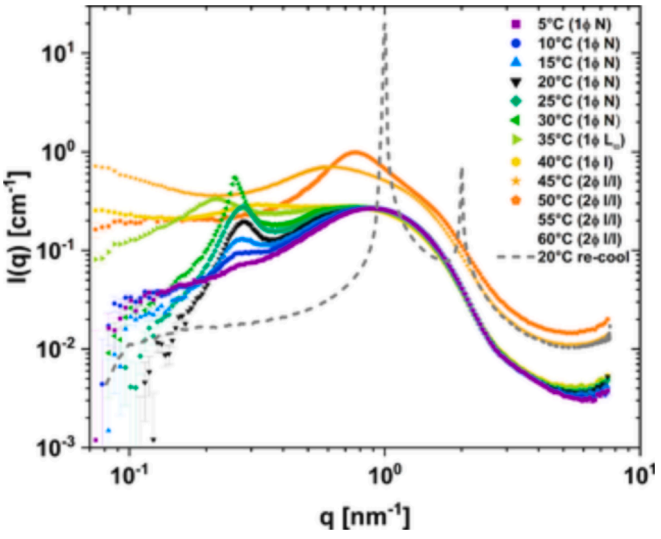

Fig. 5. SAXS data of sample 20M, containing 20 vol% surfactant mixture with R($C_{18:1}E_2CH_2COOH$) = 0.655 in H_2O, at various temperatures, taken during heating from 5 °C to 60 °C and after re-cooling to 20 °C (gray dashed line). The measured points are indicated in the phase diagrams in Figs. 2 and 3. At 5 °C to 30 °C, the sample is a nematic phase (1ϕ N). At 35 °C, a pseudo-lamellar phase (1ϕ L_α) is formed, which transitions into an isotropic phase (1ϕ I) at 40 °C. At 45 °C and above, phase separation into a dilute bottom phase and a surfactant-rich top phase (2ϕ I) occurs. Note that data for 55 °C and 60 °C are missing because the beam did not hit the surfactant-rich phase during phase separation. On another occasion, the same temperature scan, including 55 °C and 60 °C, was measured for a similar sample, see **Fig. S15**. The same temperature scans are given in **Fig. S12** for samples 15M and 25M, containing 15 vol% and 25 vol % of the surfactant mixture, respectively.

further hint at disc growth with increasing surfactant concentration may be the transition of the nematic phase to a lamellar phase around 55 wt% of surfactant, see Figs. 3 **and S7**, which can be interpreted either as 'infinite' growth of the discs to lamellae, or as a dense lamellar packing of large discs [70]. An effect of D_2O is to be expected, because D_2O shifts all phase transitions to lower temperatures, and therefore, at the same temperature, the degree of molecular segregation should vary in D_2O compared to H_2O.

Before transitioning into a pseudo-lamellar phase at 35 °C, the structure factor peak of the nematic phase becomes even sharper and its position shifts to slightly lower $q_1 = 0.257$ nm^{-1} ($D_1^* = 24.4$ nm) at 30 °C. Even a weak second order peak around $q_2 = 2 \cdot q_1$, typical for lamellar ordering [71], appears, indicating an increase in long-range order. Before intramicellar segregation into a rim and a flat part disappears completely, discs grow much larger, i.e., smaller discs merge into larger ones, resulting in a quasi-lamellar organization of large discs. When reaching the lamellar phase at 35 °C, the structure factor peak is shifted to lower $q = 0.221$ nm^{-1} ($D^* = 28.5$ nm), broadened, and no second order peak is visible. Hence, the formed lamellae are not infinite but finite undulating pseudo-lamellae with a low degree of long-range order. Undulations lead to a higher consumption of surfactant material for the same average thickness, resulting in a larger average spacing. A first evaluation to estimate the long-range order in smectics can be made by using the Scherrer relation [72]: the ratio $q_{max}/\Delta q$(FWHM), i.e., the ratio of the position of the structure factor peak maximum to the full width at half maximum (FWHM). This ratio gives the coherence length in number of layers before a defect occurs. The ratio is plotted as a function of temperature in **Fig. S10A**. The higher the ratio is, the higher is the long-range order. From 15 °C to 25 °C, the ratio is about 4 in the nematic phase, meaning that on average four bicelles are stacked before a defect occurs, increases to 7 at 30 °C, and eventually decreases to 2 when the pseudo-lamellar phase is reached at 35 °C. This progression reflects the conclusions drawn above.

It is also worth noting that the bicelles in the nematic phase can be oriented by shear. While usually no anisotropic scattering was observed in SAXS, SANS measurements of corresponding samples in D_2O, see section 3.4, at 20 °C showed significant anisotropy in scattering along the direction of applied shear during cuvette filling. For SANS, cuvettes with a thickness of 1 mm were used and cuvettes were not shaken after cuvette filling, whereas for SAXS, capillaries with a thickness of 1.5 mm were used and capillaries were shaken after filling. A 2D SANS pattern of sample d-20M, containing 20 vol% of surfactant mixture with R ($C_{18:1}E_2CH_2COOH$) = 0.655, at 20 °C is shown in **Fig. S10B**. As can be inferred from the scattering pattern, the scattered intensity is higher along the direction of cuvette filling, the highest intensity being observed in an azimuthal angle sector of 30°. This implies that the bicelles are oriented along the direction of applied shear and are mostly tilted by an angle $\varphi \leq 15°$ relative to the direction of shear, showing that the rotation of the bicelles is sufficiently hindered to retain the shear-induced orientation.

When further heating the sample to 40 °C, the pseudo-lamellar phase transforms into an isotropic phase, before at 45 °C phase separation occurs above the critical solution temperature. Within the isotropic phase, the structure factor peak flattens even more and is only weak and broad, which is a result of the loss of long-range order. The peak position is shifted to higher $q = 0.322$ nm^{-1} ($D^* = 19.5$ nm). As can also be seen in SANS data of sample d-20M at 20 °C (1ϕ N) and 33 °C (1ϕ I), given in **Fig. S11**, the form factor does not significantly change in the isotropic phase. As mentioned above, all phase boundaries are shifted to lower temperatures in D_2O, see **Fig. S8**. The SANS data at 33 °C can be fitted with a core–shell ellipsoid form factor and a simple Hayter-Penfold RMSA structure factor [58,73], see dashed line in **Fig. S11** and **Table S2**. The obtained parameters for the polar shell thickness (0.8 nm), the equatorial shell thickness (2.3 nm), and the polar core radius (2.2 nm) are similar to those obtained for the form factors of 5 vol% samples and are in agreement with the molecular dimensions, see section 3.2. The only significant difference is the equatorial core radius, which is 11.8 nm in the isotropic phase at 20 vol% surfactant at 33 °C, and therefore considerably smaller than a radius around 24 nm found in the flow-birefringent phase at 5 vol%. Note that the surfactant ratio is slightly different (R($C_{18:1}E_2CH_2COOH$) = 0.655 compared to 0.677) and the potential effect of the surfactant concentration on the disc size is unknown. For sample d-20M (D_2O), the peak of the isotropic phase at 33 °C is located at $q = 0.211$ nm^{-1} ($D^* = 29.8$ nm), while the peak position in the nematic phase at 20 °C is located at slightly higher $q = 0.259$ nm^{-1} ($D^* = 24.2$ nm). Since a repeat distance of 24.2 nm is only slightly smaller than the outer radius, including the shell, of the disc observed at 5 vol% (≈26 nm), while the sample is viscoelastic, the average disc radius must be larger than 26 nm. An outer radius, including the shell, close to 14 nm in the isotropic phase is considerably smaller than the average spacing of 29.8 nm. As a result, the discs can freely rotate, which is in agreement with the phase being isotropic. It is important to note that the peak position of the isotropic phase in SANS of sample d-20M (D_2O) is at slightly lower q than that of the nematic phase at 20 °C (**Fig. S11**), while in SAXS the peak of sample 20M (H_2O) is at slightly higher q in the isotropic phase than in the nematic phase (Fig. 5). At 33 °C, sample d-20M is very close to the phase transition from a pseudo-lamellar phase to the isotropic phase (less than 1 °C), while at 40 °C, sample 20-M is at least 1 °C further above the phase transition temperature. The same phase transitions and the same changes in SAXS were also seen for samples 15-M and 25-M, containing, respectively, 15 vol% and 25 vol% of surfactant in H_2O, see **Fig. S12**. In all cases, the peak position in the isotropic phase varies relative to the peak position of the nematic phase, and of the pseudo-lamellar phase. The peak in the isotropic phase shifts to higher q, the farther away the temperature is to the transition to a pseudo-lamellar phase. A shift to higher q corresponds to a decreasing repeat distance as a result of a decrease in average size of the micelles. The general progression of the repeat distance D*, i.e., of the structure factor peak position is identical at all three concentrations, 15, 20, and 25 vol%, and is depicted in **Fig. S13** for SAXS samples in H_2O.

At 45 °C and above, after reaching the critical clouding temperature, micelles attract each other and a surfactant-rich isotropic phase separates from an aqueous phase. With increasing temperature, the surfactant-rich phase becomes increasingly dense by expelling more and more water, which is indicated by a shift of the structure factor peak to higher q. After re-cooling the separated phases to 20 °C (dashed line in Fig. 5), the surfactant-rich top phase, containing about 65 wt% of surfactant, forms a lamellar phase made of 'infinite' sheets, much larger than the observed spacing, which is sufficiently well ordered to produce sharp first- and second-order Bragg-peaks. A comparison of SAXS of the nematic phase at 20 °C and of the metastable lamellar phase after re-cooling is also given in semi-logarithmic scale in **Fig. S14**. If the two phases are re-mixed at 20 °C by shaking, the nematic phase is formed. Note that the scattering curves of sample 20M are missing for 55 °C and 60 °C, because the beam did not hit the surfactant-rich phase. A similar series of measurements for a similar sample (see figure caption), recorded on another occasion, is given in **Fig. S15**, showing the same phase behavior, including the two higher temperatures.

3.4. *Effect of nematic gel dilution at room temperature*

In Fig. 6, the effect of dilution on the small-angle scattering of the nematic gel is depicted. SAXS of three samples 15M, 20M, and 25M, containing 15 vol%, 20 vol%, and 25 vol% of surfactant mixture with R ($C_{18:1}E_2CH_2COOH$) = 0.655 in H_2O, is shown in Fig. 6A. SANS of the corresponding samples in D_2O, d-15M, d-20M, and d–25M, containing the same volume fractions of surfactant, is shown in Fig. 6B. The repeat distance D*, extracted directly from the scattering curve, increases from 18.2 nm at 25 vol% surfactant to 22.4 nm at 20 vol% to 31.1 nm at 15 vol % in SAXS, and from 19.1 nm to 24.2 nm to 32.9 nm in SANS. As can be seen in a plot of D* versus the number density of surfactant molecules in

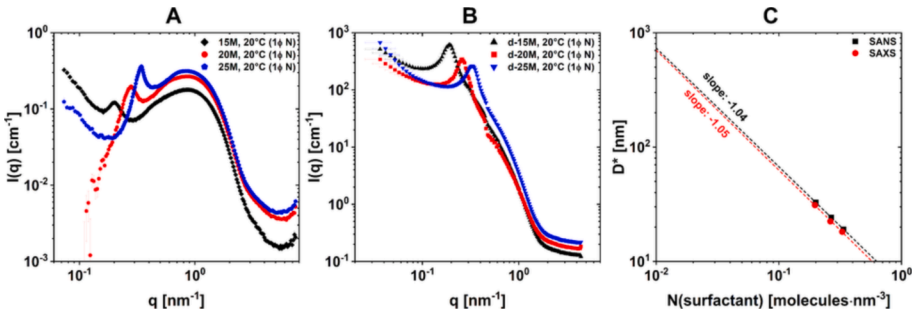

Fig. 6. (A) SAXS data of nematic gel samples 15M, 20M, and 25M at 20 °C, containing, respectively, 15 vol%, 20 vol%, and 25 vol% surfactant mixture with R($C_{18:1}E_2CH_2COOH$) = 0.655 in H_2O. The same data can be seen in the temperature series given in Figs. 5 **and S12**. (B) SANS data of corresponding nematic gel samples d-15M, d-20M, and d-25M at 20 °C, containing the same volume fractions of surfactant in D_2O with R($C_{18:1}E_2CH_2COOH$) = 0.655. (C) Repeat distance $D^* = 2\pi/q_{max}$, obtained from the peak maxima in (A) and (B), as a function of the number of surfactant molecules per unit volume N(surfactant). Dashed lines represent linear fits of the data obtained by SAXS (red points) and SANS (black squares) with slopes of −1.04 and −1.05, respectively. (For interpretation of the references to color in this figure legend, the reader is referred to the web version of this article.)

Fig. 6C, the swelling of the structures upon dilution is close to one-dimensional swelling (slopes of −1.04 and −1.05). This is in agreement with two-dimensional structures, such as the proposed stacks of large discs or lamellar structures. Due the swelling relation and since scattering curves do not significantly change apart from the structure factor, the basic structural units remain unchanged on dilution. The swelling is expected to persist to a minimum of 8 wt% of surfactant, below which the mixture loses permanent birefringence. Thus, the maximum spacing is around 60 nm, the water layer thickness being in the same order of magnitude as the bicelle diameter. The expected minimum spacing before forming a lamellar phase around 55 wt% of surfactant is close to 9 nm. Macroscopically, dilution leads to a decrease in viscosity, viscoelasticity, and eventually in birefringence. This is a result of the average spacing significantly exceeding the bicellar radius, leading to free rotation of bicelles and a loss of preferential order. To the best of our knowledge, we find here such a behavior by combining two

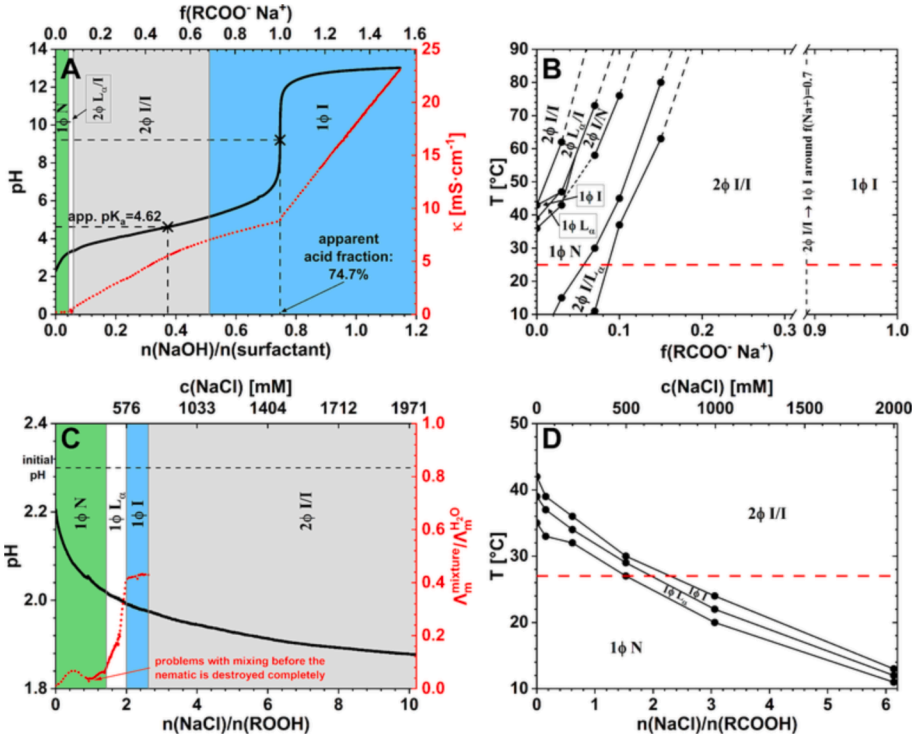

Fig. 7. (A) pH (solid black line) and specific conductivity (dotted red line) measured during titration of a 20 wt% nematic gel (R($C_{18:1}E_2CH_2COOH$) = 0.655) with 1M NaOH solution at 25 °C. Dilution due to titration leads to a progressive decrease of the surfactant content to 13.3 wt%. f($RCOO^-$ Na^+) = n($RCOO^-$ Na^+)/[n(ROOH) + n($RCOO^-$ Na^+)] is the fraction of ionic surfactants with sodium as counterion in the surfactant mixture and was corrected by the obtained apparent acid fraction of 74.7 %. (B) Phase diagram at a constant surfactant concentration of 20 wt% with R($C_{18:1}E_2CH_2COOH$) = 0.655 as a function of the degree of ionization. f($RCOO^-$ Na^+) was varied by addition of NaOH. The dashed red line is probed in the titration in (A), with the difference of a gradually decreasing surfactant concentration in (A). (C) pH (solid black line) and reduced molar conductivity (dotted red line) measured during titration of a 20 wt% nematic gel (R($C_{18:1}E_2CH_2COOH$) = 0.655) with 5M NaCl solution at 27 °C. Dilution due to titration leads to a progressive decrease of the surfactant content to 12.1 wt%. The linear bottom x-axis was calculated with an apparent acid fraction of 74.7 %, while the non-linear top x-axis gives the molar concentration of NaCl at various points. (D) Phase diagram as a function of the NaCl concentration, recorded by adding NaCl to a mixture with an initial surfactant concentration of 20 wt% with R($C_{18:1}E_2CH_2COOH$) = 0.655. The bottom x-axis gives the mole ratio of NaCl and carboxylic acid surfactants, considering an apparent acid fraction of 74.7 %, while the top x-axis gives the molar concentration of NaCl. The dashed red line is probed in the titration in (C), with the difference of a gradually decreasing surfactant concentration in (C). (For interpretation of the references to color in this figure legend, the reader is referred to the web version of this article.)

single chain surfactants for the first time. This peculiar nematic phase is only present because alkyl chains are interdigitated to produce stiffer discs, as could be demonstrated by SANS/SAXS, and because intramicellar segregation of the two surfactants is efficient. These properties probably allow for a series of formulations of low active matter content, polymer-free, self-thickening hydrogels.

As can be seen in **Fig. S16**, the magnitude of the slope of the swelling law increases with increasing temperature, which is in agreement with increasing fluctuations in bilayer thickness due to increasing intramicellar mixing, as discussed in section 3.3. The most negative slope of –1.33 is observed in the undulating pseudo-lamellar phase, indicating the "loss" of material due to undulations, according to the Helfrich model [74]. In the isotropic phase, the slope increases to −0.89 as a result of smaller discs no longer swelling in one dimension only, since the distance between neighboring discs in their equatorial plane can no longer be neglected. Note that the slope in the isotropic phase is also influenced by the change in micellar size, depending on the exact position in the isotropic domain of the phase diagram, see section 3.3.

3.5. Effect of NaOH and NaCl on the nematic gel

In Fig. 7A, the pH and specific conductivity measured during titration of a sample containing 20 wt% surfactant ($R(C_{18:1}E_2CH_2COOH)$ = 0.655) with 1M NaOH solution at 25 °C are given. A phase diagram versus temperature and the degree of ionization at a constant surfactant content of 20 wt% with $R(C_{18:1}E_2CH_2COOH)$ = 0.655 is shown in Fig. 7B. As can be seen in both Fig. 7A and 7B, introducing electrostatics by deprotonation of the surfactants' carboxylic acid moieties destabilizes the nematic phase. Despite the total surfactant concentration decreasing to 13.3 wt% over the course of the titration in Fig. 7A, the phase transitions are almost identical compared to a constant surfactant concentration in Fig. 7B. At 25 °C, deprotonating only 5 % of the surfactants leads to the disappearance of the nematic phase. First, a biphasic region with an isotropic top phase and a lamellar bottom phase occurs, before two isotropic phases are formed above 8 % of deprotonation. When reaching a deprotonation of around 70 %, the mixture becomes a single isotropic phase of low viscosity. This phase sequence suggests that making the headgroups increasingly ionic results in a structural transition towards increasingly globular micelles, as electrostatic repulsion between adjacent headgroups leads to an increase in area per headgroup, and therefore to a decrease of the spontaneous packing parameter. Up to around 15 % of deprotonation, the introduced electrostatic repulsion can be compensated by headgroup dehydration on increasing temperature. Around 15 % of deprotonation a temperature of at least 90 °C is required to form the nematic phase. Despite the high temperature, the mixtures appear to be strongly viscoelastic. Note that the obtained apparent acid fraction of 74.7 mol% of the surfactant mixture, calculated using the average molar masses of the surfactants, is lower than the apparent acid fraction of around 82 mol% found for $C_8E_8CH_2COOH$ (**Fig. S1**). This is in agreement with the higher content of nonionic ester impurities expected for $C_{18:1}E_2CH_2COOH$, see section 2.1 and **Note S2**.

The pH and reduced molar conductivity of a mixture initially containing 20 wt% of surfactant with $R(C_{18:1}E_2CH_2COOH)$ = 0.655 measured at 27 °C during titration with a 5M NaCl solution is given in Fig. 7C. A phase diagram as a function of temperature and NaCl concentration, obtained by addition of NaCl to a mixture with an initial surfactant concentration of 20 wt% with $R(C_{18:1}E_2CH_2COOH)$ = 0.655, is given in Fig. 7D. NaCl has a salting-out effect on the surfactant mixture, decreasing the phase transition temperatures by dehydrating the surfactant headgroups without altering the phase sequence. The nematic phase is stable up to at least 0.6M NaCl at room temperature, and thus should be formed even in sea water [75]. The initial decrease of the pH by around 0.3 pH units is partially a result of H^+ release as Na^+ partially replaces H^+ as a counterion of the carboxylate groups. At higher NaCl concentrations, the pH electrode reading is influenced by the salt, resulting in up to 0.2 pH units lower readings [76]. The reduced molar conductivity, i.e., the ratio of the molar conductivity of the mixture and the molar conductivity of brine containing the same salt concentration, is below 0.1 in the viscous nematic gel, and sharply increases in the pseudo-lamellar phase until it reaches a value of around 0.4 in the isotropic phase. A relative water self-diffusion of around 0.5 [77] and a reduced conductivity of around 0.5 [78] were reported for 10 vol% to 20 vol% of a L_3 sponge phase formed by $C_{12}E_5$. The relative water self-diffusion typically found in a micellar L_1 phase of globular nonionic micelles of similar volume fraction is between 0.7 and 0.8 [79]. However, as pointed out by Photinos and Saupe [80], a slightly perforated lamellar structure and a layered structure of discs are not easily distinguishable in terms of conductivity. Thus, it can be expected that conductivities of an isotropic phase containing relatively large discs and an isotropic sponge phase are similar as well.

The important conclusions to be drawn from this investigation are the limiting salt concentrations for a possible viscosity control strategy using salt, as commonly applied for sodium dodecyl sulfate (SDS) or sodium dodecylbenzenesulfonate (SDBS), and that the nematic gel can be transformed into standard globular micelles by adding 0.5 NaOH. It should also be noted that NaOH and NaCl have opposing effects on curvature, the former increasing it by introducing electrostatic repulsion, and the latter decreasing it by dehydrating headgroups and screening electrostatics. Thus, the nematic phase can also be tweaked by combining the additions of NaOH and NaCl.

4. Molecular segregation controlling bicellar size

As discussed in section 3, intramicellar molecular segregation is the reason for bicelle formation. $C_{18:1}E_2CH_2COOH$ favors a low curvature, adopting lamellar packing, while $C_8E_8CH_2COOH$ favors a high curvature, adopting spherical packing [48]. The former tendency is expressed in the formation of a L_β phase in binary mixtures of $C_{18:1}E_2CH_2COOH$ and water, see Fig. 1A. On mixing of the two surfactants, $C_8E_8CH_2COOH$ forms curved rims, limiting the size of the $C_{18:1}E_2CH_2COOH$ bilayers. The resulting shape is a bicelle, as sketched in Fig. 8, in which the two surfactants are segregated. To quantify segregation, one can introduce separate surfactant mole fractions for the bilayer disc and the spheroidal rim.

The mole fraction $x_{disc}(C_8E_8CH_2COOH) = n_{disc}(C_8E_8CH_2COOH)/[n_{disc}(C_8E_8CH_2COOH) + n_{disc}(C_{18:1}E_2CH_2COOH)]$ is the mole fraction of $C_8E_8CH_2COOH$ in the flat disc part, while $x_{rim}(C_{18:1}E_2CH_2COOH)$ is the mole fraction of $C_{18:1}E_2CH_2COOH$ in the spheroidal rim. For complete intramicellar segregation, $x_{disc}(C_8E_8CH_2COOH) = 0$ and $x_{rim}(C_{18:1}E_2CH_2COOH) = 0$, while for full intramicellar mixing the mole fractions are given by $R(C_{18:1}E_2CH_2COOH)$, where $x_{disc}(C_8E_8CH_2COOH) = 1 - R(C_{18:1}E_2CH_2COOH)$ and $x_{rim}(C_{18:1}E_2CH_2COOH) = R(C_{18:1}E_2CH_2COOH)$. For a given composition of the surfactant mixture, the bicellar dimensions can be calculated as a function of $x_{disc}(C_8E_8CH_2COOH)$ and $x_{rim}(C_{18:1}E_2CH_2COOH)$, see **Note S5**. For $R(C_{18:1}E_2CH_2COOH)$ = 0.706, the calculated values of the bicellar hydrophobic core radius R_{core} are given as a function of $x_{disc}(C_8E_8CH_2COOH)$ and $x_{rim}(C_{18:1}E_2CH_2COOH)$ in Fig. 8. In the case of full intramicellar mixing, indicated as a green line in Fig. 8, the core radius diverges and cannot be predicted. The opposite case of complete intramicellar segregation would produce bicelles with R_{core} = 10.3 nm, significantly smaller than $R_{core} \approx 24$ nm obtained from SANS fits, see **Fig. S9**. Complete intramicellar segregation is only a hypothetical state, as a certain degree of mixing of the two surfactants is to be expected due to the entropy of mixing. For a core radius of 24 nm at 20 °C, indicated as a blue plane in Fig. 8**A, a** variety of disc and rim compositions would be feasible, as can be derived by considering the intersection of the plane with the possible values for R_{core} (black surface in Fig. 8A). The possible combinations of the two compositions can be seen in the graph as a projection of the intersection to the $x_{disc}(C_8E_8CH_2COOH)$-$x_{rim}(C_{18:1}E_2CH_2COOH)$-plane (blue line). High values of

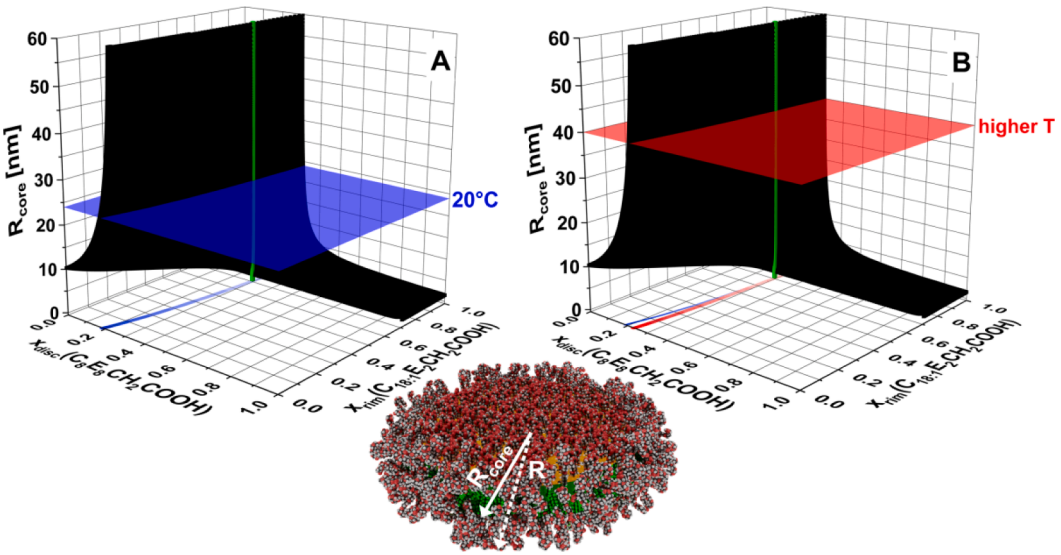

Fig. 8. Calculated hydrocarbon core radius R_{core} of a bicelle consisting of a flat cylindrical disc and a spheroidal rim as a function of the surfactant mole fractions $x_{disc}(C_8E_8CH_2COOH)$ and $x_{rim}(C_{18:1}E_2CH_2COOH)$. $x_{disc}(C_8E_8CH_2COOH) = 1 - x_{disc}(C_{18:1}E_2CH_2COOH)$ describes the mole fraction of $C_8E_8CH_2COOH$ in the flat disc, and $x_{rim}(C_{18:1}E_2CH_2COOH) = 1 - x_{rim}(C_8E_8CH_2COOH)$ describes the mole fraction of $C_{18:1}E_2CH_2COOH$ in the spheroidal rim. In the calculations, see **Note S5**, the solvent-free hydrophobic core is considered. Thus, both mole fractions only take into account the two surfactants. A total surfactant composition as in samples 5M_a_0.706 and d-5M_a_0.706 is assumed ($R(C_{18:1}E_2CH_2COOH) = 0.706$). The vertical green line indicates, where $x_{disc}(C_8E_8CH_2COOH) = 1 - R(C_{18:1}E_2CH_2COOH)$ and $x_{rim}(C_{18:1}E_2CH_2COOH) = R(C_{18:1}E_2CH_2COOH) = 0.706$, i.e., where the two surfactants fully mix. At these points, the calculation of R_{core} diverges and R_{core} cannot be predicted. A scaled model of a bicelle with full intramicellar segregation is also shown. (For interpretation of the references to color in this figure legend, the reader is referred to the web version of this article.)

$x_{rim}(C_{18:1}E_2CH_2COOH)$ are unrealistic, as that would imply a preference of $C_{18:1}E_2CH_2COOH$ for high curvature. Thus, the most probable combinations of $x_{disc}(C_8E_8CH_2COOH)$ and $x_{rim}(C_{18:1}E_2CH_2COOH)$ are those with low values of $x_{rim}(C_{18:1}E_2CH_2COOH)$, which is indicated by a more intense color of the blue line. If the rims are made predominantly of $C_8E_8CH_2COOH$, i.e., if $x_{rim}(C_{18:1}E_2CH_2COOH) \approx 0$, the predicted disc composition for a core radius of 24 nm would be $x_{disc}(C_{18:1}E_2CH_2COOH) \approx 0.8 > R(C_{18:1}E_2CH_2COOH)$.

An increase in temperature facilitates intramicellar mixing, reducing the volume fraction of rims limiting the bicellar size, thus increasing its core radius. This is visualized in Fig. 8B, where the red plane indicates an arbitrarily chosen core radius of 40 nm at elevated temperature. The possible rim and disc compositions for $R_{core} = 40$ nm are given as a red line in Fig. 8B, where the blue line for $R_{core} = 24$ nm is also shown for comparison. To increase R_{core}, $x_{disc}(C_8E_8CH_2COOH)$ has to increase, i.e., more $C_8E_8CH_2COOH$ has to be removed from the rim and mixed into the disc. For $x_{rim}(C_{18:1}E_2CH_2COOH) \approx 0$, $x_{disc}(C_{18:1}E_2CH_2COOH)$ would decrease from around 0.8 at 20 °C to around 0.75. Note that the required change of $x_{disc}(C_8E_8CH_2COOH)$ to increase R_{core} would decrease with increasing $x_{rim}(C_{18:1}E_2CH_2COOH)$, as a state of full intramicellar mixing would be approached.

(A) The blue plane indicates R_{core} at 20 °C, as obtained from a fit of the SANS data of sample d-5M_a to a core–shell ellipsoid form factor, see Fig. S9A. The intersection of the blue plane and the black surface (R_{core}) is shown as a projection to the $x_{disc}(C_8E_8CH_2COOH)$-$x_{rim}(C_{18:1}E_2CH_2COOH)$-plane (blue line) and yields the possible combinations of $x_{disc}(C_8E_8CH_2COOH)$ and $x_{rim}(C_{18:1}E_2CH_2COOH)$ to obtain a bicelle with $R_{core} = 24$ nm. The darker color of the blue line at lower values of $x_{rim}(C_{18:1}E_2CH_2COOH)$ indicates that larger values for $x_{rim}(C_{18:1}E_2CH_2COOH)$ are unlikely. (B) The red plane indicates R_{core} at a higher temperature, where R_{core} was arbitrarily chosen to be 40 nm. In addition to the blue $x_{disc}(C_8E_8CH_2COOH)$-$x_{rim}(C_{18:1}E_2CH_2COOH)$ projection from (A), the intersection of the red plane and the black surface (R_{core}) is shown as a projection to the $x_{disc}(C_8E_8CH_2COOH)$-$x_{rim}(C_{18:1}E_2CH_2COOH)$-plane (red line) and yields the possible combinations of $x_{disc}(C_8E_8CH_2COOH)$ and $x_{rim}(C_{18:1}E_2CH_2COOH)$ to obtain a bicelle with $R_{core} = 40$ nm.

5. Conclusion and outlook

Synthetic (lipid-free), almost uncharged bicelles are formed by mixing $C_8E_8CH_2COOH$ and $C_{18:1}E_2CH_2COOH$ in appropriate ratios R ($C_{18:1}E_2CH_2COOH$). The bicelles are formed due to intramicellar segregation of the two surfactants into a high curvature rim, favored by $C_8E_8CH_2COOH$, and a flat disc, favored by $C_{18:1}E_2CH_2COOH$. The bicellar size at a given surfactant composition is controlled by the degree of intramicellar segregation, which is influenced by temperature. For the compositions investigated by small-angle scattering at room temperature, typical bicelle diameters are around 50 nm. In sufficient number, above 8 wt% of surfactant, the bicelles form a discotic viscoelastic nematic phase with a maximum swelling of 60 nm. The nematic phase is surrounded by various lamellar phases. Above 55 wt% of surfactant, bicelles either fully merge into 'infinite' lamellae or only partially merge to form a lamellar-like stack of large discs [70]. On decreasing R ($C_{18:1}E_2CH_2COOH$) below the limit of the nematic phase, molecular segregation is intermicellar, resulting in phase separation of a $C_{18:1}E_2CH_2COOH$-rich lamellar phase and a $C_8E_8CH_2COOH$-rich isotropic phase. On increasing $R(C_{18:1}E_2CH_2COOH)$ or temperature, the nematic phase transitions into a pseudo-lamellar phase of large undulating discs, followed by an isotropic phase of smaller disc-like micelles, and eventually phase separation occurs on reaching the critical solution temperature. The latter is the classical clouding phenomenon observed for ethoxylated nonionic surfactants [52]. After phase separation above the critical temperature, there is a metastable state of a concentrated lamellar top phase and a dilute isotropic bottom phase after re-cooling, which returns to the nematic equilibrium state on mixing the two phases. This should allow for a formulation of a concentrated lamellar phase as a precursor to the viscoelastic nematic phase, achievable by simple dilution.

Two possible applications of nematic phases of swollen bicelles were tested:

(a) Incorporation of droplets of apolar hydrocarbon oils by dispersion in the nematic phase. However, even when adding very apolar oils (high oil/water partition coefficient logP value) such

as squalane, the nematic phase disappears. An exemplary phase map obtained by successive addition of squalane to a nematic gel containing 20 wt% surfactant with R($C_{18:1}E_2CH_2COOH$) = 0.643 is given in **Fig. S17**. A small amount of squalane (≈3 wt%) is solubilized in the nematic phase, before a transition to a lamellar phase, followed by a transition to a microemulsion, is induced. The microemulsion is stable up to around 12 wt% squalane, above which phase separation occurs. The solubilization performance tends to increase with increasing R($C_{18:1}E_2CH_2COOH$) within the nematic phase, e.g., the nematic phase and the microemulsion persist up to 7 wt% and 20 wt% squalane, respectively, at R($C_{18:1}E_2CH_2COOH$) = 0.688.

(b) We have evaluated the threshold between infinite entrapment and floating of air bubbles introduced by simple shaking by hand as described in the experimental section 2.9. Considering the dynamic range of radii of air bubbles that could be tracked between 190 µm and 1070 µm, a slope of −1 is evidenced in Fig. 9. This shows that the floating is driven by defects in the nematic phase. To the best of our knowledge, the nematic phase is the first fully open structure that shows a threshold without closed microcapsules, thus enabling capsule-free encapsulation. A nematic phase with similar properties but made of sheets consisting of small prolate micelles linked by carboxylic acid dimerization [81] instead of large discs, thus requiring fatty acids as linkers, was recently reported by Tchakalova et al. [43]. Since the disc radius is typically 25 nm, air bubbles with a diameter of 1 mm have a threshold linked to the number of defects in 1 mm^3 of sample. The number of defects is also linked to the color bands shown in the polarized image of a nematic gel shown in Fig. 2**A**. By extrapolation of the data in Fig. 9, we expect a threshold for floating of an object of 8 µm radius to be of the order of 300 Pa. Transposing this to typical capsules in this size range and a conservative value of fragrance density of 0.8 $g{\cdot}cm^{-3}$, suggests that entrapment of such capsules would persist up to typical ultracentrifugation. These values show that the threshold in Pa is sufficient to encapsulate objects for a very long time, until shaking or temperature increase releases objects from the shear thinning nematic phase that is stable up to 34 °C in the examined case.

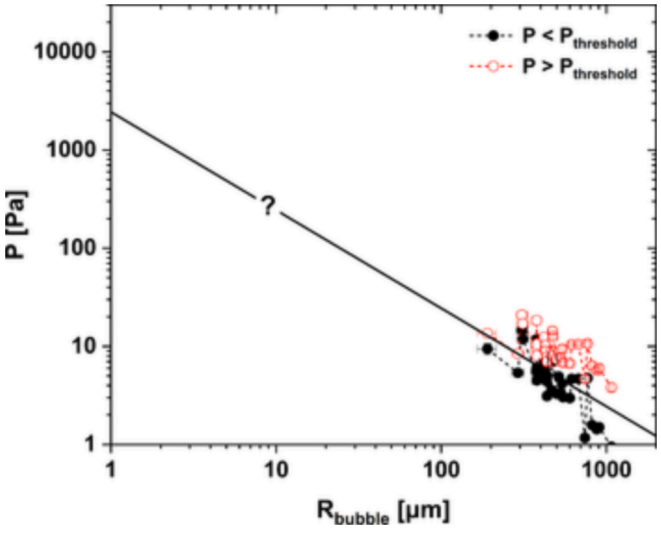

Fig. 9. Testing entrapment of air bubbles in a nematic gel containing 20 wt% surfactant mixture with R($C_{18:1}E_2CH_2COOH$) = 0.655 at 25 °C. It reveals the size dependence of the threshold between full entrapment and floating, determined by progressive soft centrifugation.

The investigated nematic gels can be loaded with oils, but have a relatively low performance in solubilization of oils compared to other microemulsions [82,83]. They are good for encapsulating air bubbles as well as any micron sized objects other than liquids that influence phase behavior. Note that the low pH (≈2.2) of the presented nematic gels can be limiting for the selection of dispersible materials. However, we recently observed that the same nematic gel can be achieved without carboxylic acid groups, i.e., with $C_{18:1}E_2$ and C_8E_8, in which case the pH can be freely varied. On the other hand, the presence of the carboxylic acid groups allows for the implementation of at least a few percent of counterions, which could potentially extend the field of application, e.g., to magnetic properties and catalysis. The nematic gel is easy to handle since the viscosity is low when shear is applied. At zero shear, on the other hand, viscosity is 'infinite', and the relaxation time for structure restoration after applied shear is negligible (<1 s), see also **Video S1**. This should make mixing with high pressure homogenizers very easy. In addition, any solute released from an entrapped capsule is free to move by diffusion in a totally continuous aqueous phase and does not have to cross multiple bilayers in an uncontrolled way.

Other known gels used for encapsulating micron sized objects are made of densely packed multilamellar vesicles (MLVs) formed in a variety of charged and uncharged surfactant systems, mostly by applying shear to a lamellar phase [84]. Such MLVs can possess viscoelastic gel-like behavior similar to that of the herein reported nematic gel [39–41], even with a yield stress comparable to the first yield stress found in this work (≈ 1 Pa) [39]. Other reported discotic nematic phases on the other hand are usually not or only weakly viscoelastic [22,35,36,85]. The viscoelasticity in this system could be a result of the relatively high volume fraction of large discs (radius ≥ 25 nm, aspect ratio ≥ 10) with strongly hydrated headgroups.

In our system, combining $C_8E_8CH_2COOH$ and $C_{18:1}E_2CH_2COOH$, the presence of MLVs can be excluded as there are no higher order peaks in the small-angle scattering of the nematic phase, which are usually observed for MLVs [39,86–88], and at the same time linear swelling is observed, which would not be expected for MLVs with too few layers to produce higher order peaks. Further, Maltese crosses that are typically observed in polarizing microscopy for MLVs [89–91] were not seen in the nematic phase. In the pseudo-lamellar regime, there is strong static birefringence that could only be observed if onion-like vesicles are of the same size as the wavelength of light. In this phase, it should be possible to produce MLVs by shearing or in extrusion processes used to mix components in industry.

Funding

This research did not receive any specific grant from funding agencies in the public, commercial, or not-for-profit sectors.

CRediT authorship contribution statement

Patrick Denk: Writing – original draft, Visualization, Validation, Methodology, Investigation, Formal analysis, Conceptualization. **Lauren Matthews:** Validation, Methodology, Investigation, Formal analysis. **Sylvain Prévost:** Validation, Methodology, Investigation, Formal analysis. **Thomas Zemb:** Writing – review & editing, Supervision, Conceptualization. **Werner Kunz:** Writing – review & editing, Supervision, Conceptualization.

Declaration of competing interest

The authors declare that they have no known competing financial interests or personal relationships that could have appeared to influence the work reported in this paper.

Data availability

Data will be made available on request.

Acknowledgement

The authors thank the ESRF, France and the ILL, France for granting beam time. The authors also thank Kao Chemicals GmbH, in particular Dr. Thomas Myrdek, for providing the surfactants free of charge and for sharing information about the surfactants. Further, the authors are grateful to Prof. Dr. Michael Gradzielski for helpful discussions.

Appendix A. Supplementary data

Supplementary data to this article can be found online at https://doi.org/10.1016/j.jcis.2024.01.014.

References

[1] C.R. Sanders, J.P. Schwonek, Characterization of magnetically orientable bilayers in mixtures of dihexanoylphosphatidylcholine and dimyristoylphosphatidylcholine by solid-state NMR, Biochemistry 31 (1992) 8898–8905, https://doi.org/10.1021/bi00152a029.
[2] G. Raffard, S. Steinbruckner, A. Arnold, J.H. Davis, E.J. Dufourc, Temperature−Composition Diagram of Dimyristoylphosphatidylcholine−Dicaproylphosphatidylcholine “Bicelles” Self-Orienting in the Magnetic Field. A Solid State 2 H and 31 P NMR Study, Langmuir 16 (2000) 7655–7662, https://doi.org/10.1021/la000564g.
[3] M.-P. Nieh, C.J. Glinka, S. Krueger, R.S. Prosser, J. Katsaras, SANS Study of the Structural Phases of Magnetically Alignable Lanthanide-Doped Phospholipid Mixtures, Langmuir 17 (2001) 2629–2638, https://doi.org/10.1021/la001567w.
[4] J. Katsaras, T.A. Harroun, J. Pencer, M.-P. Nieh, “Bicellar” Lipid Mixtures as Used in Biochemical and Biophysical Studies, Naturwissenschaften 92 (2005) 355–366, https://doi.org/10.1007/s00114-005-0641-1.
[5] J.N. Israelachvili, D.J. Mitchell, B.W. Ninham, Theory of self-assembly of hydrocarbon amphiphiles into micelles and bilayers, J. Chem. Soc., Faraday Trans. 2: Mol. Chem. Phys. 72 (1976) 1525–1568, https://doi.org/10.1039/F29767201525.
[6] R.R. Vold, R.S. Prosser, A.J. Deese, Isotropic solutions of phospholipid bicelles: A new membrane mimetic for high-resolution NMR studies of polypeptides, J Biomol NMR. 9 (1997) 329–335, https://doi.org/10.1023/a:1018643312309.
[7] E.J. Dufourc, Bicelles and nanodiscs for biophysical chemistry, Biochim. Biophys. Acta (BBA) – Biomembr. 1863 (2021) 183478, https://doi.org/10.1016/j.bbamem.2020.183478.
[8] L. Barbosa-Barros, G. Rodríguez, C. Barba, M. Cócera, L. Rubio, J. Estelrich, C. López-Iglesias, A. de la Maza, O. López, Bicelles: Lipid Nanostructured Platforms with Potential Dermal Applications, Small 8 (2012) 807–818, https://doi.org/10.1002/smll.201101545.
[9] K.S. Mineev, K.D. Nadezhdin, S.A. Goncharuk, A.S. Arseniev, Characterization of Small Isotropic Bicelles with Various Compositions, Langmuir 32 (2016) 6624–6637, https://doi.org/10.1021/acs.langmuir.6b00867.
[10] P.M. Macdonald, R. Soong, Diffusion NMR and bicelle morphology, Can J Chem. 89 (2011) 1021–1035, https://doi.org/10.1139/v11-038.
[11] R. Soong, M.-P. Nieh, E. Nicholson, J. Katsaras, P.M. Macdonald, Bicellar Mixtures Containing Pluronic F68: Morphology and Lateral Diffusion from Combined SANS and PFG NMR Studies, Langmuir 26 (2010) 2630–2638, https://doi.org/10.1021/la902795h.
[12] L. van Dam, G. Karlsson, K. Edwards, Direct observation and characterization of DMPC/DHPC aggregates under conditions relevant for biological solution NMR, Biochim. Biophys. Acta (BBA) – Biomembr. 1664 (2004) 241–256, https://doi.org/10.1016/j.bbamem.2004.06.005.
[13] C. Loudet-Courreges, F. Nallet, E.J. Dufourc, R. Oda, Unprecedented Observation of Days-Long Remnant Orientation of Phospholipid Bicelles: A Small-Angle X-ray Scattering and Theoretical Study, Langmuir 27 (2011) 9122–9130, https://doi.org/10.1021/la1050817.
[14] S.H. Park, S.J. Opella, Triton X-100 as the “Short-Chain Lipid” Improves the Magnetic Alignment and Stability of Membrane Proteins in Phosphatidylcholine Bilayers for Oriented-Sample Solid-State NMR Spectroscopy, J Am Chem Soc. 132 (2010) 12552–12553, https://doi.org/10.1021/ja1055565.
[15] S. Taguchi, Y. Kimura, Y. Akiyama, Y. Tachibana, T. Yamamoto, Fluorescent Anisotropy Evaluation of Bicelle Formation Employing Carboxyl BODIPY and Pyrromethene, J Oleo Sci. 71 (2022) ess21295, https://doi.org/10.5650/jos.ess21295.
[16] K.D. Lawson, T.J. Flautt, Magnetically oriented lyotropic liquid crystalline phases, J Am Chem Soc. 89 (1967) 5489–5491, https://doi.org/10.1021/ja00997a054.
[17] L.Q. Amaral, C.A. Pimentel, M.R. Tavares, J.A. Vanin, Study of a magnetically oriented lyotropic mesophase, J Chem Phys. 71 (1979) 2940–2945, https://doi.org/10.1063/1.438696.
[18] B.J. Forrest, F.Y. Fujiwara, L.W. Reeves, Order profiles of host decyl sulfate and decylammonium chains and guest carboxylic acids and carboxylates in aligned type II DM lyomesophases, J Phys Chem. 84 (1980) 662–670, https://doi.org/10.1021/j100443a019.
[19] E.Y. Sheu, P. Lo Nostro, G. Capuzzi, P. Baglioni, Micelle and Microemulsion Properties of Cesium Di-Dodecyl-Dimethylsulfosuccinate, Cs-AOT, Langmuir 15 (1999) 6671–6676, https://doi.org/10.1021/la990059n.
[20] H.-D. Dörfler, C. Görgens, Mizellpolymorphie lyotroper Mesophasen, Tenside Surfactant Deterg. 36 (1999) 314–321, https://doi.org/10.1515/tsd-1999-360509.
[21] C.F. Dietrich, P. Rudquist, K. Lorenz, F. Giesselmann, Chiral Structures from Achiral Micellar Lyotropic Liquid Crystals under Capillary Confinement, Langmuir 33 (2017) 5852–5862, https://doi.org/10.1021/acs.langmuir.7b01074.
[22] G. Colafemmina, R. Recchia, A.S. Ferrante, S. Amin, G. Palazzo, Lauric Acid-Induced Formation of a Lyotropic Nematic Phase of Disk-Shaped Micelles, J Phys Chem b. 114 (2010) 7250–7260, https://doi.org/10.1021/jp1020774.
[23] L.J. Yu, A. Saupe, Observation of a Biaxial Nematic Phase in Potassium Laurate-1-Decanol-Water Mixtures, Phys Rev Lett. 45 (1980) 1000–1003, https://doi.org/10.1103/PhysRevLett.45.1000.
[24] S.E. Anachkov, P.A. Kralchevsky, K.D. Danov, G.S. Georgieva, K. P. Ananthapadmanabhan, Disclike vs. cylindrical micelles: Generalized model of micelle growth and data interpretation, J Colloid Interface Sci. 416 (2014) 258–273, https://doi.org/10.1016/j.jcis.2013.11.002.
[25] N. Boden, S.A. Corne, K.W. Jolley, Lyotropic mesomorphism of the cesium pentadecafluorooctanoate/water system: high-resolution phase diagram, J Phys Chem. 91 (1987) 4092–4105, https://doi.org/10.1021/j100299a031.
[26] D. Danino, Cryo-TEM of soft molecular assemblies, Curr Opin Colloid Interface Sci. 17 (2012) 316–329, https://doi.org/10.1016/j.cocis.2012.10.003.
[27] M. Dubois, V. Lizunov, A. Meister, T. Gulik-Krzywicki, J.M. Verbavatz, E. Perez, J. Zimmerberg, T. Zemb, Shape control through molecular segregation in giant surfactant aggregates, Proc. Natl. Acad. Sci. 101 (2004) 15082–15087, https://doi.org/10.1073/pnas.0400837101.
[28] M. Dubois, L. Belloni, T.h. Zemb, B. Demé, T.h. Gulik-Krzywicki, Formation of rigid nanodiscs: edge formation and molecular separation, in: Trends in Colloid and Interface Science XIV, Springer, Berlin Heidelberg, Berlin, Heidelberg, 2000, pp. 238–242, https://doi.org/10.1007/3-540-46545-6_47.
[29] A. Meister, M. Dubois, L. Belloni, T. Zemb, Equation of State of Self-Assembled Disklike and Icosahedral Crystallites in the Dilute Range, Langmuir 19 (2003) 7259–7263, https://doi.org/10.1021/la0346806.
[30] M. Dubois, T. Gulik-Krzywicki, B. Demé, T. Zemb, Rigid organic nanodisks of controlled size: A catanionic formulation, Comptes Rendus de l’Académie Des Sciences - Series IIC - Chemistry 1 (1998) 567–575, https://doi.org/10.1016/S1387-1609(98)80012-1.
[31] B.J. Forrest, L.W. Reeves, New lyotropic liquid crystals composed of finite nonspherical micelles, Chem Rev. 81 (1981) 1–14, https://doi.org/10.1021/cr00041a001.
[32] V. Hendrikx, J. Charvolin, M. Rawiso, L. Liebert, M.C. Holmes, Anisotropic aggregates of amphiphilic molecules in lyotropic nematic phases, J Phys Chem. 87 (1983) 3991–3999, https://doi.org/10.1021/j100243a039.
[33] Y. Hendrikx, J. Charvolin, Structural relations between lyotropic phases in the vicinity of the nematic phases, J. Phys. 42 (1981) 1427–1440, https://doi.org/10.1051/jphys:0198100420100142700.
[34] M.C. Holmes, D.J. Reynolds, N. Boden, Concentration-temperature dependence of the size and shape of the micelles in the cesium pentadecafluorooctanoate/water system, J Phys Chem. 91 (1987) 5257–5262, https://doi.org/10.1021/j100304a025.
[35] D. Venkata Sai, G. Mirri, P.H.J. Kouwer, R. Sahoo, I. Musevic, S. Dhara, Unusual temperature dependence of elastic constants of an ambient-temperature discotic nematic liquid crystal, Soft Matter 12 (2016) 2960–2964, https://doi.org/10.1039/C6SM00065G.
[36] L.R.P. de Andrade Lima, A.D. Rey, Linear viscoelasticity of discotic mesophases, Chem Eng Sci. 59 (2004) 3891–3905, https://doi.org/10.1016/j.ces.2004.06.016.
[37] A. Nikzad, A. Akbari, D. Grecov, Rheological properties of discotic nematic liquid crystals: graphene oxide dispersions study, Liq Cryst. 48 (2021) 1685–1698, https://doi.org/10.1080/02678292.2021.1897890.
[38] C.L.S. Risi, A.M. Figueiredo Neto, P.R.G. Fernandes, A.R. Sampaio, E. Akpinar, M.B. L. Santos, Shear viscosity and rheology of ternary and quaternary lyotropic liquid crystals in discotic and calamitic nematic phases, Rheol Acta. 54 (2015) 529–543, https://doi.org/10.1007/s00397-015-0850-2.
[39] R. Abdel-Rahem, M. Gradzielski, H. Hoffmann, A novel viscoelastic system from a cationic surfactant and a hydrophobic counterion, J Colloid Interface Sci. 288 (2005) 570–582, https://doi.org/10.1016/j.jcis.2005.03.040.
[40] H. Hoffmann, C. Thunig, P. Schmiedel, U. Munkert, Surfactant Systems with Charged Multilamellar Vesicles and Their Rheological Properties, Langmuir 10 (1994) 3972–3981, https://doi.org/10.1021/la00023a013.
[41] M. Gradzielski, The rheology of vesicle and disk systems — Relations between macroscopic behaviour and microstructure, Curr Opin Colloid Interface Sci. 16 (2011) 13–17, https://doi.org/10.1016/j.cocis.2010.07.005.
[42] P.-G. de Gennes, J. Prost, The Physics of Liquid Crystals, 2nd ed., Clarendon Press, Oxford, 1993.
[43] V. Tchakalova, C.L.P. Oliveira, A.M. Figueiredo Neto, New Lyotropic Complex Fluid Structured in Sheets of Ellipsoidal Micelles Solubilizing Fragrance Oils, ACS Omega. (2023). https://doi.org/10.1021/acsomega.3c03500.
[44] F. Cattelaens, M. Jäger, T. Myrdek, Purification of carboxymethylated fatty alcohol derivates using ion exchange resins, J Surfactants Deterg. 26 (2023) 111–117, https://doi.org/10.1002/jsde.12641.
[45] R. Kjellander, E. Florin, Water structure and changes in thermal stability of the system poly(ethylene oxide)–water, Journal of the Chemical Society, Faraday

Trans. 1: Phys. Chem. Condens. Phases. 77 (1981) 2053. https://doi.org/10.1039/f19817702053.
[46] O. Tirosh, Y. Barenholz, J. Katzhendler, A. Priev, Hydration of polyethylene glycol-grafted liposomes, Biophys J. 74 (1998) 1371–1379, https://doi.org/10.1016/S0006-3495(98)77849-X.
[47] C. Branca, S. Magazù, G. Maisano, F. Migliardo, P. Migliardo, G. Romeo, Hydration Study of PEG/Water Mixtures by Quasi Elastic Light Scattering, Acoustic and Rheological Measurements, J Phys Chem b. 106 (2002) 10272–10276, https://doi.org/10.1021/jp014345v.
[48] P. Denk, A. El Maangar, J. Lal, D. Kleber, T. Zemb, W. Kunz, Phase diagrams and microstructures of aqueous short alkyl chain polyethylene glycol ether carboxylate and carboxylic acid triblock surfactant solutions, J Colloid Interface Sci. 590 (2021) 375–386, https://doi.org/10.1016/j.jcis.2021.01.061.
[49] P. Denk, A. El Maangar, S. Prévost, W. Silva, R. Gschwind, T. Zemb, W. Kunz, Cloud point, auto-coacervation, and nematic ordering of micelles formed by ethylene oxide containing carboxylate surfactants, J Colloid Interface Sci. 621 (2022) 470–488, https://doi.org/10.1016/j.jcis.2022.04.046.
[50] C.D. Dewhurst, Graphical reduction and analysis small-angle neutron scattering program: GRASP, J Appl Crystallogr. 56 (2023) 1595–1609, https://doi.org/10.1107/S1600576723007379.
[51] W.H. Herschel, R. Bulkley, Konsistenzmessungen von Gummi-Benzollösungen, Kolloid-Zeitschrift 39 (1926) 291–300, https://doi.org/10.1007/BF01432034.
[52] D.J. Mitchell, G.J.T. Tiddy, L. Waring, T. Bostock, M.P. McDonald, Phase behaviour of polyoxyethylene surfactants with water. Mesophase structures and partial miscibility (cloud points), J. Chem. Soc., Faraday Trans. 1: Phys. Chem. Condens. Phases 79 (1983) 975. https://doi.org/10.1039/f19837900975.
[53] T. Zemb, P. Charpin, Micellar structure from comparison of X-ray and neutron small-angle scattering, J. Phys. 46 (1985) 249–256, https://doi.org/10.1051/jphys:01985004602024900.
[54] A. Krężel, W. Bal, A formula for correlating pKa values determined in D2O and H2O, J Inorg Biochem. 98 (2004) 161–166, https://doi.org/10.1016/j.jinorgbio.2003.10.001.
[55] L.S. Ornstein, F. Zernike, Accidental deviations of density and opalescence at the critical point of a single substance, Proc. Akad. Sci. (Amsterdam) XVII (1914) 793–806.
[56] M. Doucet, J.H. Cho, G. Alina, Z. Attala, J. Bakker, W. Bouwman, P. Butler, K. Campbell, T. Cooper-Benun, C. Durniak, L. Forster, M. Gonzalez, R. Heenan, A. Jackson, S. King, P. Kienzle, J. Krzywon, R. Murphy, T. Nielsen, L. O'Driscoll, W. Potrzebowski, S. Prescott, R. Ferraz Leal, P. Rozyczko, T. Snow, A. Washington, SasView, (2021). https://doi.org/10.5281/zenodo.4467703.
[57] V. Degiorgio, M. Corti, Physics of Amphiphiles: Micelles, Vesicles and Microemulsions: Proceedings of the International School of Physics, Enrico Fermi, Course XC, Elsevier Science Pub. Co., Amsterdam, New York, 1985.
[58] J. Hansen, J.B. Hayter, A rescaled MSA structure factor for dilute charged colloidal dispersions, Mol Phys. 46 (1982) 651–656, https://doi.org/10.1080/00268978200101471.
[59] L. Chiappisi, S. David Leach, M. Gradzielski, Precipitating polyelectrolyte–surfactant systems by admixing a nonionic surfactant – a case of cononsurfactancy, Soft Matter 13 (2017) 4988–4996, https://doi.org/10.1039/C7SM00747G.
[60] M. Schwarze, L. Chiappisi, S. Prévost, M. Gradzielski, Oleylethoxycarboxylate – An efficient surfactant for copper extraction and surfactant recycling via micellar enhanced ultrafiltration, J Colloid Interface Sci. 421 (2014) 184–190, https://doi.org/10.1016/j.jcis.2014.01.037.
[61] P. Alexandridis, U. Olsson, B. Lindman, Self-Assembly of Amphiphilic Block Copolymers, Macromolecules 28 (1995) 7700–7710.
[62] L.M. Bergström, S. Skoglund, K. Edwards, J. Eriksson, I. Grillo, Spontaneous Transformations between Surfactant Bilayers of Different Topologies Observed in Mixtures of Sodium Octyl Sulfate and Hexadecyltrimethylammonium Bromide, Langmuir 30 (2014) 3928–3938, https://doi.org/10.1021/la4042259.
[63] K. Emelyanova, I. Gotlib, A. Shishkina, M. Voznesenskiy, A. Victorov, Molecular Thermodynamic Modeling of Self-Assembly into Branches and Spatial Networks in Solution, J Chem Eng Data. 61 (2016) 4013–4022, https://doi.org/10.1021/acs.jced.6b00531.
[64] K.A. Emelyanova, A.I. Victorov, Driving Force for Spontaneous Perforation of Bilayers Formed by Ionic Amphiphiles in Aqueous Salt, Langmuir 33 (2017) 13438–13443, https://doi.org/10.1021/acs.langmuir.7b02885.
[65] K.A. Emelyanova, A.I. Victorov, Molecular thermodynamic modeling of a bilayer perforation in mixed catanionic surfactant systems, PCCP 20 (2018) 27924–27929, https://doi.org/10.1039/C8CP04593C.
[66] M. Almgren, Stomatosomes: perforated bilayer structures, Soft Matter 6 (2010) 1383, https://doi.org/10.1039/b922707e.
[67] C. Tanford, Micelle shape and size, J. Phys. Chem. 76 (1972) 3020–3024, https://doi.org/10.1021/j100665a018.
[68] S. Abrahamsson, I. Ryderstedt-Nahringbauer, The crystal structure of the low-melting form of oleic acid, Acta Crystallogr. 15 (1962) 1261–1268, https://doi.org/10.1107/S0365110X62003321.
[69] F. Kaneko, K. Yamazaki, K. Kitagawa, T. Kikyo, M. Kobayashi, Y. Kitagawa, Y. Matsuura, K. Sato, M. Suzuki, Structure and Crystallization Behavior of the β Phase of Oleic Acid, J Phys Chem b. 101 (1997) 1803–1809, https://doi.org/10.1021/jp963400a.
[70] M. Dubois, D. Carrière, R. Iyer, M.A. Arunagirinathan, J. Bellare, J.M. Verbavatz, T. Zemb, From dispersed nanodiscs to thin films of layered organic material via reversible swelling, Colloids Surf A Physicochem Eng Asp. 319 (2008) 90–97, https://doi.org/10.1016/j.colsurfa.2007.05.051.
[71] O. Glatter, in: Scattering Methods and their Application in Colloid and Interface Science, 1st ed., Elsevier, Amsterdam, 2018 https://doi.org/10.1016/C2016-0-04640-5.
[72] P. Scherrer, Bestimmung der Größe und der inneren Struktur von Kolloidteilchen mittels Röntgenstrahlen, Nachrichten Von Der Gesellschaft Der Wissenschaften Zu Göttingen, Mathematisch-Physikalische Klasse 1918 (1918) 98–100. http://eudml.org/doc/59018.
[73] J.B. Hayter, J. Penfold, An analytic structure factor for macroion solutions, Mol Phys. 42 (1981) 109–118, https://doi.org/10.1080/00268978100100091.
[74] F. Campelo, C. Arnarez, S.J. Marrink, M.M. Kozlov, Helfrich model of membrane bending: From Gibbs theory of liquid interfaces to membranes as thick anisotropic elastic layers, Adv Colloid Interface Sci. 208 (2014) 25–33, https://doi.org/10.1016/j.cis.2014.01.018.
[75] F.J. Millero, R. Feistel, D.G. Wright, T.J. McDougall, The composition of Standard Seawater and the definition of the Reference-Composition Salinity Scale, Deep Sea Res. Part I 55 (2008) 50–72, https://doi.org/10.1016/j.dsr.2007.10.001.
[76] G. Hinds, P. Cooling, A. Wain, S. Zhou, A. Turnbull, Technical Note: Measurement of pH in Concentrated Brines, Corrosion 65 (2009) 635–638, https://doi.org/10.5006/1.3319089.
[77] B. Balinov, U. Olsson, O. Soederman, Structural similarities between the L3 and bicontinuous cubic phases in the AOT-brine system, J Phys Chem. 95 (1991) 5931–5936, https://doi.org/10.1021/j100168a041.
[78] R. Strey, R. Schomäcker, D. Roux, F. Nallet, U. Olsson, Dilute lamellar and L 3 phases in the binary water–C12E5 system, J. Chem. Soc., Faraday Trans. 86 (1990) 2253–2261, https://doi.org/10.1039/FT9908602253.
[79] P.G. Nilsson, B. Lindman, Water self-diffusion in nonionic surfactant solutions. Hydration and Obstruction Effects, J Phys Chem. 87 (1983) 4756–4761, https://doi.org/10.1021/j100246a041.
[80] P.J. Photinos, A. Saupe, Calculations on the electric conductivity of a lyotropic mesophase with perforated lamellae, J Chem Phys. 81 (1984) 563–566, https://doi.org/10.1063/1.447338.
[81] J. Chen, C.L. Brooks, H.A. Scheraga, Revisiting the carboxylic acid dimers in aqueous solution: Interplay of hydrogen bonding, hydrophobic interactions and entropy, J. Phys. Chem. B 112 (2008) 242–249, https://doi.org/10.1021/jp074355h.
[82] M.L. Klossek, D. Touraud, W. Kunz, Microemulsions with renewable feedstock oils, Green Chem. 14 (2012) 2017, https://doi.org/10.1039/c2gc35035a.
[83] K. Ozawa, U. Olsson, H. Kunieda, Oil-Induced Structural Change in Nonionic Microemulsions, J Dispers Sci Technol. 22 (2001) 119–124, https://doi.org/10.1081/DIS-100102687.
[84] K. Mortensen, Structural studies of lamellar surfactant systems under shear, Curr Opin Colloid Interface Sci. 6 (2001) 140–145, https://doi.org/10.1016/S1359-0294(01)00071-1.
[85] S.K. Ghosh, V. Rathee, R. Krishnaswamy, V.A. Raghunathan, A.K. Sood, Re-entrant phase behavior of a concentrated anionic surfactant system with strongly binding counterions, Langmuir 25 (2009) 8497–8506, https://doi.org/10.1021/la804330x.
[86] P. Heftberger, B. Kollmitzer, F.A. Heberle, J. Pan, M. Rappolt, H. Amenitsch, N. Kučerka, J. Katsaras, G. Pabst, Global small-angle X-ray scattering data analysis for multilamellar vesicles: the evolution of the scattering density profile model, J Appl Crystallogr. 47 (2014) 173–180, https://doi.org/10.1107/S1600576713029798.
[87] P. Saveyn, J. Cocquyt, M. Gradzielski, P. Van der Meeren, Osmotic effects on the enclosed volume and interlamellar spacing of multilamellar DODAC vesicles, Colloids Surf A Physicochem Eng Asp. 319 (2008) 62–70, https://doi.org/10.1016/j.colsurfa.2007.03.046.
[88] J.I. Escalante, M. Gradzielski, H. Hoffmann, K. Mortensen, Shear-Induced Transition of Originally Undisturbed Lamellar Phase to Vesicle Phase, Langmuir 16 (2000) 8653–8663, https://doi.org/10.1021/la000242c.
[89] M. Genty, G. Couarraze, R. Laversanne, C. Degert, L. Navailles, T. Gulik-Krzywicki, J.-L. Grossiord, Characterization of a complex dispersion of multilamellar vesicles, Colloid Polym Sci. 282 (2003) 32–40, https://doi.org/10.1007/s00396-003-0907-0.
[90] S. Khodaparast, W. Sharratt, H. Wang, E.S.J. Robles, R. Dalgliesh, J.T. Cabral, Spontaneous formation of multilamellar vesicles from aqueous micellar solutions of sodium linear alkylbenzene sulfonate (NaLAS), J Colloid Interface Sci. 546 (2019) 221–230, https://doi.org/10.1016/j.jcis.2019.03.056.
[91] R. Abdel-Rahem, Effect of Glycerol on the Swelling of Multilamellar Vesicles Composed of Cetyltrimethylammonium Bromide and Sodium Hydroxy-Naphthoate, J Dispers Sci Technol. 32 (2011) 784–794, https://doi.org/10.1080/01932691.2010.488131.